International Journal of Thermofluids 24 (2024) 100857

Contents lists available at ScienceDirect

International Journal of Thermofluids

journal homepage: www.sciencedirect.com/journal/international-journal-of-thermofluids

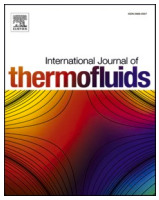

# Thermal-induced buoyant water jet discharge under shallow coastal water conditions

Amir Bordbar [a,*], Yong Ming Dai [a], Simone Michele [a], Ola Zawalna-Geer [b], Zhengwei Chen [c,d], Salah A Faroughi [e], Yeaw Chu Lee [a]

[a] School of Engineering, Computing and Mathematics, University of Plymouth, PlymouthPL4 8AA, UK
[b] Faculty of Environment, Science and Economy, University of Exeter, Penryn TR10 9FE, UK
[c] National Rail Transit Electrification and Automation Engineering Technology Research Center (Hong Kong Branch), Hong Kong, China
[d] Department of Civil and Environmental Engineering, The Hong Kong Polytechnic University, Hong Kong, China
[e] Department of Chemical Engineering, University of Utah, Salt Lake City, Utah 8412, USA

ARTICLE INFO

*Keywords:*
Thermal-induced jet flow
Computational fluid dynamics
Discharge dispersion modelling
Multiphase flow
Wave-current environment
Laboratory experiment

ABSTRACT

A novel discharge dispersion model is developed to simulate the complex three-dimensional flow behaviour of thermal-induced buoyant water jets under current-wave coexisting conditions. The model solved the governing fluid flow and energy equations for two immiscible and incompressible phases (water and air) which were weakly coupled by applying the Boberbeck-Boussinesq approximation. Different turbulence models, such as k−ε multiphase, k-ω SST, k-ω SST-multiphase, k-ω SST-stable, and realizable k−ε were applied. Extensive verification of the model's performance is conducted by comparing the developed model results against a diverse range of analytical and experimental data. First, a series of simulations are carried out to evaluate the performance of the model in reproducing the results of the wave hydrodynamic and interactions with the submerged trapezoid bar. This is followed by numerically replicating the experimental results of a vertical non-buoyant submerged jet under current-only and current-wave environments. Finally, the potency of the coupled hydro-thermal algorithm is assessed by validating against different thermal-induced buoyant submerged jet experimental tests. For this purpose, numerical prediction of the developed model is tested against physical experiments for a series of tests for thermal-induced buoyant submerged horizontal jets in stationary water and inclined thermal-induced buoyant water jet under the influence of current-wave environments. Results showed that the k-ω SST-multiphase provides the best agreement with the laboratory measured data in terms of flow, temperature distribution field, plume trajectory and dilution. The findings confirmed that the developed model can be used as a reliable tool in precisely modelling characteristic of thermal-induced buoyant water jet in shallow coastal waters.

## 1. Introduction

The growth and deployment of large-scale Waterbodies Thermal Energy Based Systems (WTEBSs) (i.e. seawater air-conditioning, surface water heat pump, and ocean energy thermal conversion systems or their combinations) raise concerns about their adverse impacts on sustainability to marine environments and ecosystems. During their operation, these systems discharge a large volume of water into the surrounding environment which can potentially change water characteristics and consequently affect marine ecosystems [1–3].

In shallow water WTEBSs that represent systems that abstract surface water, the returning fluid is discharged into the shallow water which maintains the same qualities (e.g. salinity and nutrient loading) but has different temperatures [4]. This temperature gradient enhances the potential of change in near-field water temperature which may have an extreme effect on local marine ecology [4–7]. A control measure to avoid this adverse impact is to achieve maximum effluent mixing efficiency which requires a full understanding of the behaviour of WTEBS discharge mixing zone in coastal water environments.

From the pertinent literature, numerical and experimental investigations on the characteristics of the submerged jets in non-stationary environments (i.e. wave-current flow condition) have been extensively covered. In these studies, the mixing behaviour of jet plumes in near-field dilution, *P*, can be derived from the effective variables

* Corresponding author.
*E-mail addresses:* abordbar182@gmail.com, amir.bordbar@plymouth.ac.uk (A. Bordbar).

https://doi.org/10.1016/j.ijft.2024.100857

Available online 16 September 2024

**Table 1**
advantages and disadvantages of numerical models in simulation of submerged jet into non-stationary environment [4].

| Submerged jet into nonstationary flow modelling | Advantages | Disadvantages |
|---|---|---|
| [9] and Yu et al. [10] | - Simulate seawater temperature field in two-dimensional field | - Can only be applied in shallow water<br>- Lack of validation<br>- No buoyancy effect modelling |
| Chen et al. [11] | Consider buoyancy effect<br>Validated against laboratory data | - Only valid under wave condition with no current flow |
| Pat Grandelli et al. [12] | Large-scale modelling<br>Consider buoyancy effect<br>Capable of biological modelling | - Only designed for OTEC systems - Not applicable for shallow water modelling |
| Kim and Kim [13] | - Can reproduce the plume behaviour in coastal water | - Lack of validation |
| JETLAG/VISJET [14], VISUAL PLUMES [15], COREJET/CORMIX Jirka and Domeker [16] | - Capable of fast prediction of mixing zone characteristics - Platform for mixing zone modelling | - Insensitive in predicting the influence of crossflow direction on jet behaviour<br>- Commercial software |
| Xu et al. [17], Xu et al. [8], Xu et al. [18], and Xu et al. [19] | - Simulate jet flow under different combination of current and wave conditions | - No temperature distribution modelling |
| FANG et al. [20] | - Predict the characteristic behaviour of a buoyant jet in a wavy crossflow environment | - No temperature distribution modelling |

associated with the water jet and the surrounding water as a function of,

$$P = f\left(U_j,\ d,\ h,\ \Delta\rho,\ D,\ U_a,\ \theta\right) \tag{1}$$

where $U_j$ is the jet flow speed, $d$ is the hydraulic diameter of the nozzle, $h$ is nozzle outlet height from the seabed, Δρ density difference between the discharge and ambient water which can be classified as a positive-, negative-, or non-buoyant flow (e.g. salinity or thermal-induced buoyancy), $D$ is water depth, $U_a$ ambient current-wave flow velocity, and θ is the angle between the discharge and ambient flow direction [8]. Nevertheless, a very limited number of studies were focused on the thermal-induced buoyancy jet flow into non-stationary environments. Bordbar et al. [4] provide a comprehensive review of the research in the field and revealed the lack of a comprehensive and sophisticated computational fluid dynamics (CFD) model to simulate the hydro-thermal behaviour of thermal-induced effluents in shallow waters under combined current-wave conditions. A non-exclusive list of the advantages and disadvantages of the numerical investigations on effluent dispersion into non-stationary environments is supplied in Table 1.

The present study aims to bridge this knowledge gap by providing a novel discharge dispersion modelling tool that can be applied for studying near-field jet dilution and plume trajectory of discharged water from shallow water WTEBS. The model numerically solves the governing hydro-thermal equations to simulate the characteristics of thermal-induced turbulent jet under shallow water coastal environments. A broad range of analytical and experimental data from the literature were taken to verify the hydrodynamic and hydro-thermal capabilities of the model. This is followed by validation with physical model experiment developed at the COAST laboratory at the University of Plymouth, to accurately predict and model inclined buoyant hot-water jet under the influence of currents and waves. The next section details the applied numerical model setup and the governing equations. In Section 3, the results of validation against a range of hydrodynamic and hydro-thermal data are presented. Finally, in the conclusion section, the findings of this study are summarised.

## 2. Description of the numerical model

The developed solver is capable of simulating submerged buoyant water jets discharged into the marine environment under current and wave conditions. The model is developed for cases where the discharged fluid is water with different temperatures to that of the ambient water. Therefore, the discharge water has the same properties of the ambient water, and the only contribution for buoyancy effect is from the difference in the water volume due to temperature gradient (i.e. thermal-induced flow). This is typical the case for the returning water into the sea or lake in shallow water-based ocean thermal energy systems. Interested readers are referred to Bordbar et al. [4], for more information regarding WTEBSs.

### 2.1. Governing equations

A hydro-thermal model is developed using OpenFOAM®. An available solver for solving two immiscible and incompressible phase flow, interFoam, was chosen as the base for the model development. The fluid flow and energy equations were weakly coupled by applying the Boberbeck-Boussinesq approximation; this approximation theory assumes that variation in fluid properties due to temperature change are negligible except for density, whereas the density variation only appears in terms that represent buoyancy effect.

From the viewpoint of environmental hydraulics, the discharge water from WTEBS into marine environments can be characterised in the form of a turbulent jet. Therefore, the flow field including two phases of water and air was governed by using the incompressible Reynolds Averaged Navier-Stokes (RANS) equations, which has a proven capability in modelling of most coastal engineering practical applications via solving the following system of conservation equations,

$$\nabla.\boldsymbol{u} = 0 \tag{2}$$

$$\frac{\partial\rho\boldsymbol{u}}{\partial t} + \nabla.\left[\rho\boldsymbol{u}\boldsymbol{u}^T\right] = -\nabla p + \nabla.\left[(\mu+\mu_t)\nabla\boldsymbol{u}\right] + \rho_T\boldsymbol{g} + \sigma_T\kappa\nabla\alpha \tag{3}$$

where ρ is density, $\boldsymbol{u}$ is the velocity vector, $p$ is the pressure, $\boldsymbol{g}$ is gravitational acceleration vector, and μ is molecular dynamic viscosity; $\mu_t$ is turbulent dynamic viscosity which is calculated by the chosen turbulence model, $\sigma_T$ is surface tension constant and κ is the curvature of water-air interface. Note that α is the indicator phase function to define the quantities of phases per unit of volume at each computational cell, which is defined as a value between 0 and 1, where $\alpha = 0$ imply that the cell consists of only air, conversely when $\alpha = 1$ the cell is fulfilled with water. Any other values represent the air-water interface (i.e. $0 < \alpha < 1$). Based on this definition, water-air property, ∅, at each computational cells for the mixture are calculated using,

$$\varnothing = \alpha\varnothing_w + (1-\alpha)\varnothing_a \tag{4}$$

where $\varnothing_w$, and $\varnothing_a$ are water and air properties, respectively. The tracking of the two immiscible phases of water-air interface is done using an adapted Volume of Fluid (VoF) method in OpenFOAM® as follows,

$$\frac{\partial\alpha}{\partial t} + \nabla.[\alpha\boldsymbol{u}] + \nabla.[\boldsymbol{u}_r\alpha(1-\alpha)] = 0 \tag{5}$$

where $\boldsymbol{u}_r$ is an interface compression velocity to suppress the diffusive behaviour of the interface [21,22]. $\rho_T$, in Eq. (3), is the density function of temperature to encompass the impact of density changes in gravitational term for water phase, which is defined by,

$$\rho_T = \alpha\rho_{w,0}[1-\beta(T-T_0)] + (1-\alpha)\rho_{air} \tag{6}$$

where β is coefficient of volume expansion for water, $T$ is the temperature, and $\rho_{w,0}$, $T_0$ are density and temperature of the water phase for a reference point, respectively.

The energy conservation equation is also computed, given by,

$$\frac{\partial \rho c_p T}{\partial t} + \nabla.[\rho c_p \boldsymbol{u} T] = \nabla^2[kT] \tag{7}$$

where $k$ and $c_p$ are thermal conductivity and specific heat capacities of the mixtures, respectively. However, discretising the energy equation in this format produces a persistent instability and unbounded growth of temperature field in the water-air interface as a consequence of sharp jumps in material properties at the interface. Hence, a more stable form of the energy equation is implemented in the code, as follows,

$$\frac{\partial \rho T}{\partial t} + \nabla.[\rho \boldsymbol{u} T] = \nabla.\left[\, k \,/\, c_p \nabla T\right]. \tag{8}$$

Eq. (8) is valid if $c_p$ is constant or is assumed a weak function of temperature.

A finite volume numerical discretisation method is used to discretize the governing equations in the computational fields. The Pressure Implicit with Splitting of Operators (PISO) algorithm, by Ferziger et al. [23] and Issa [24] was applied for the pressure-velocity calculation procedure. The discretization of temporal terms was carried out using the mixed Euler and Crank-Nicolson schemes. The mixed schemes used a coefficient, $c$, for blending function where $c = 0$ is pure Euler, and $c = 1$ is Crank-Nicolson; following Weller et al. [22], $c = 0.9$ is recommended for a good compromise between accuracy and robustness.

### 2.2. Wave generation and absorption boundaries

To be able to reproduce the laboratory wavemaker velocity profiles in a numerical wave tank (NWT), a specific boundary conditions for wave propagation and wave breaking is required. Recently, different methods for numerical wave generator and absorber have been developed in OpenFOAM® that is supported in interFoam. Jacobsen et al. [25] implemented a toolbox, wave2Foam that utilised a generic wave generation and absorption method known as wave relaxation zones. A main disadvantage of this method is that the existence of a wave damping region produces an increment of mean water levels [26,27]. The other drawback of this method is that extending the computational domain for relaxation zones adds up to increased computational cost. Higuera et al. [26], Higuera et al. [28] and Higuera [29] further developed the IHFoam/OlaFlow toolbox. This toolbox has a wave generator boundary that included all the widely used theories plus specific piston-type wavemaker replication and an active wave absorption boundary using linear shallow water theory to dissipate the outgoing waves. The active wave absorber has a good capability in improving solution stability and presenting very low reflection coefficients, however its capability in absorbing large amplitude waves is controversial [30]. Mohseni and Soares [30] suggested using cell stretching wave damping technique as a supplement to olaFlow active wave absorption to ensure suppression of wave reflections. Using the cell stretching technique, a mesh stretching zone is defined before the outlet where the spatial discretization in the wave direction is gradually increased towards the outlet boundary which filters any wavelengths shorter that the cell size [30,31]. Applying porous media tool available in OpenFOAM® by Hafsteinsson [32] as a porous beach has also been employed for wave dissipation in Dao et al. [33].

In the present study, the developed hydro-thermal model was integrated with the olaFlow tool to produce a solver that can mimic the discharge of submerged buoyant water jet into the marine environment with current and wave conditions.

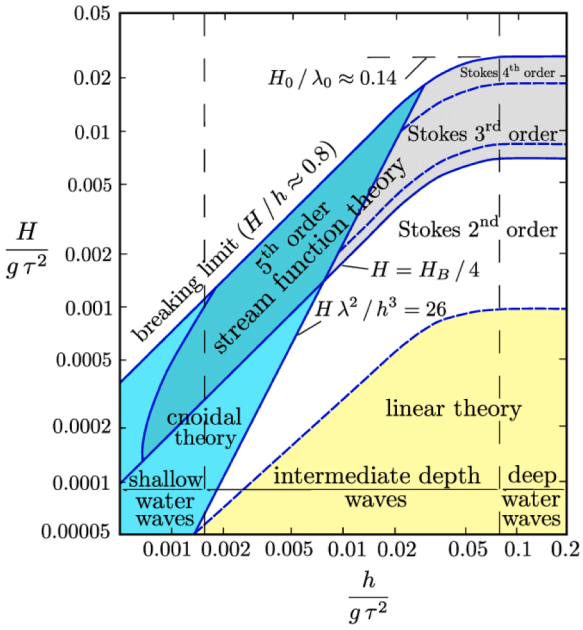


**Fig. 1.** Limits of validity for various wave theories by Le Méhauté [34].

## 3. Validation and results

### 3.1. Hydrodynamic modelling

This section aims to validate the developed model against unsteady free-surface flow subjected to gravitational forces known as water waves. Water wave motions are extremely diverse and complex to define and any mathematical definition of them is corresponded to idealized situations that never occur exactly but are only approximated [34]. Fig. 1 shows a well-known diagram of two-dimensional periodic waves by Le Méhauté [34] that describes the validity of different regular wave theories that are dependent on the relative water depth ($H/g\tau^2$) and the wave steepness ($h/g\tau^2$), where $H$ is wave height, $h$ is static water depth, and τ is wave period. A pure two-dimensional wave motion does not exist, but it is a convenient way to mathematical define physics of water waves in a tank with parallel walls, such as those observed in a long fluid flume [34].

In this study, four different turbulence closure models (k-ω SST, k−ε multiphase, k-ω SST-multiphase, k-ω SST-stable) are considered to investigate the wave hydrodynamics and their interactions with the submerged trapezoid bar, see, test cases 3.1.1 to 3.1.4. k-ω SST is chosen for its proven capability in predicting adverse pressure gradient and separating flow [35]. In the other hand, k−ε multiphase, and k-ω SST-multiphase are variants built on the standard k−ε and k-ω SST models in OpenFOAM® for multiphase flows [29]. It is noted that the default version of incompressible turbulence models in OpenFOAM® are not designed for multiphase flow modelling, due to the density has being considered constant [29]. Finally, the k-ω SST-stable turbulence closure model is selected for its capability in predicting wave surface elevations, as well as turbulence and undertow velocity profiles [36].

The applied boundaries for the flow parameters of the two-dimensional computational domains are listed in Table 2. A wave generator and wave absorber, as defined in olaflow, were employed at the inlet and outlet, respectively. This involved specifying Dirichlet boundary conditions for the free surface (VoF function) and velocity components at the inlet, while applying an active wave absorber at the outlet. The bottom and top boundaries are satisfied using OpenFOAM built-in boundary conditions; top boundary is resolved with an open atmosphere boundary and no-slip is used for the bottom boundary and the turbulence properties are treated using different wall functions for

**Table 2**
Applied boundary condition for two-dimensional flow modelling test cases.

| Boundaries | FrontAndBack | Top (patch/atmospheric) | Bottom/ Pipe wall (no-slip wall) | Inlet (wave generator) | Outlet (wave absorber) |
|---|---|---|---|---|---|
| Velocity ($u$) | empty | pressureInletOutletVelocity | fixedValue | waveVelocity | waveAbsorbtion |
| Pressure ($p$) | empty | totalPressure | zeroGradient | zeroGradient | zeroGradient |
| Phase fraction ($\alpha$) | empty | inletOutlet | zeroGradient | waveAlpha | zeroGradient |
| Turbulent kinetic energy ($k$) | empty | inletOutlet | kqRWallFunction | fixedValue | inletOutlet |
| Turbulent dissipation ($\varepsilon$) | empty | inletOutlet | epsilonWallFunction | fixedValue | inletOutlet |
| Specific turbulent dissipation rate ($\omega$) | empty | inletOutlet | omegaWallFunction | fixedValue | inletOutlet |
| Kinematic turbulent viscosity ($\nu_t = \mu_t/\rho$) | empty | calculated | nutkWallFunction | calculated | Calculated |

**Table 3**
Specifications of the applied linear wave.

| Period $\tau$ ($s$) | Wave amplitude $H$ ($m$) | Water depth $h$ ($m$) | Wave number $k$ ($m^{-1}$) | Wavelength $L$ ($m$) |
|---|---|---|---|---|
| 2 | 0.02 | 1 | 1.2039 | 5.2163 |

smooth-surfaces, see Cebeci and Bradshaw [37] and Cebeci and Chang [38] with respect to the applied turbulence models.

In the following, the results of hydrodynamic modelling using the developed model in comparison with results of several analytical models and experimental data from the literature is provided.

### 3.1.1. Generation and propagation of the linear wave

The linear wave theory provides the simplest analytical solution for regular waves which are sinusoidal with constant wave height ($H$), wavelength ($L$) and wave period ($\tau$) [39]. Despite of the easy implementation, linear wave theory, known as Stokes I or Airy wave theory, is accurate and practical for wide range of engineering applications [29]. Here, water is assumed to be incompressible, inviscid and its motion irrotational. In this case, the motion of gravity waves on a fluid surface can be described using potential flow [40]. Other assumptions are that the surface tension is negligible and the pressure at the free-surface is constant. The bottom is fixed and impermeable and wave height is relatively small ($H/h \ll 1$) [41,29]. For a two-dimensional Airy wave propagating in $x$-direction, the free surface displacement and velocity components ($u$, $w$) in $x$- and $z$- direction as described in Dean and Dalrymple [42] are:

$$\eta(t,x) = \frac{H}{2}\cos(\theta) \tag{9}$$

$$u(t,x) = \frac{H}{2}\omega\frac{\cosh(kz)}{\sinh(kh)}\cos(\theta) \tag{10}$$

$$w(t,x) = \frac{H}{2}\omega\frac{\sinh(kz)}{\sinh(kh)}\sin(\theta) \tag{11}$$

$$\theta = kx - \omega t + \psi \tag{12}$$

where $k$ is wave number, $\omega$ is angular frequency, and $\psi$ is wave phase shift. Angular frequency is calculated using,

$$\omega = \frac{2\pi}{T} \tag{13}$$

and wave number calculated using dispersion relation for water waves,

$$\omega^2 = gk\tanh(kh) \tag{14}$$

where $g$ is acceleration of gravity.

A linear wave with the specifications in Table 3 is employed. It is noted that using the wave theories (e.g. Stokes I) outside of their range of applicability may cause wave decomposition in simulation, as equilibrium cannot be satisfied [29].

For the simulation, a 2D rectangular computational domain, 30 $m$ long and 2 $m$ height, is created. Finer grid cells are considered near the free-surface interface area to ensure any disturbances are captures accurately. A mesh dependency study was conducted employing k-$\omega$ SST-multiphase turbulence model with four different mesh resolutions, as listed in Table 4. For each case, the Root Mean Squared Error (RMSE) as a standard deviation of the residual was used to compare the deviation of the simulation outcomes from the analytical data for time evolution of the surface elevation in a specific distance from the inlet wave generator boundary. The outcomes indicated a high level of mesh independence, particularly for cases with fine and very fine mesh resolutions. The very fine mesh (mesh with $420 \times 10^3$ grid cells) was chosen for the simulations as shown in Fig. 2, where the red and blue colour shows the initial phase distribution field for water and air, respectively.

**Table 4**
Mesh dependency study for linear wave theory simulations.

| Mesh resolution | Number of cells | Smallest cell size ($m^2$) | RMSE (-) |
|---|---|---|---|
| Very coarse | $160 \times 10^3$ | $0.02 \times 0.01$ | 0.04086 |
| Coarse | $238 \times 10^3$ | $0.015 \times 0.007$ | 0.02059 |
| Fine | $325 \times 10^3$ | $0.012 \times 0.006$ | 0.01682 |
| Very fine | $420 \times 10^3$ | $0.01 \times 0.005$ | 0.01547 |

The simulation results, in terms of the time evolution of the surface elevation of propagating waves, were compared with analytical solutions at four different distances from the inlet of the computational domain(i.e. $x = 0.5L, 1L, 2L, 3L$), as shown in Fig. 3 to see the impact of distance from the wave generator boundary in propagating wave characteristics. In general, no evidence of wave reflection from the wave active absorber could be detected in the results. In all cases, good agreement between CFD and analytical results are observed, however, with long progression in time and distance from the wave generator boundary, small variations from the analytical solution could be seen. These variations are more visible in Fig. 3d where k-$\omega$ SST and k-$\omega$ SST-multiphase models yield more precise results compared to the other solutions.

### 3.1.2. Generation and propagation of the non-linear stokes II wave

Stokes in 1847 for the first time established the nonlinear solution using the perturbation theory for the regular waves, known as Stokes expansion [43]. Based on this Stokes expansion, the relevant equations for the Stokes II wave surface displacement and velocity components are described by adding the second order (quadratic) term into linear wave theory as follows:

$$\eta(t,x) = \frac{H}{2}\cos(\theta) + k\frac{H^2}{4}\frac{3-\tanh^2(kh)}{4\tanh^3(kh)}\cos(2\theta) \tag{15}$$

$$u(t,x) = \frac{H}{2}\omega\frac{\cosh(kz)}{\sinh(kh)}\cos(\theta) + \frac{3}{4}\frac{H^2\omega k\cosh(2kz)}{4\sinh^4(kh)}\cos(2\theta) \tag{16}$$

$$w(t,x) = \frac{H}{2}\omega\frac{\sinh(kz)}{\sinh(kh)}\sin(\theta) + \frac{3}{4}\frac{H^2\omega k\sinh(2kz)}{4\sinh^4(kh)}\sin(2\theta) \tag{17}$$

The specification for the simulated non-linear Stokes II wave theory is listed in Table 5 .

For this test case, a similar two-dimensional rectangular

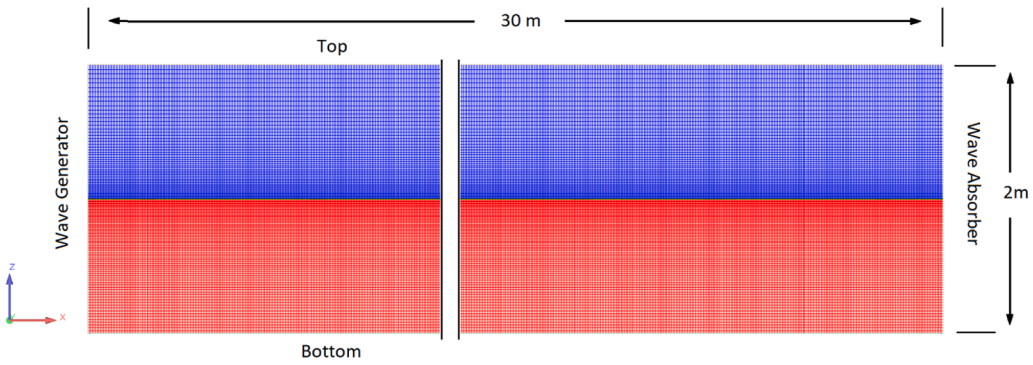


**Fig. 2.** Generate mesh with red and blue colours representing water and air phases, respectively.

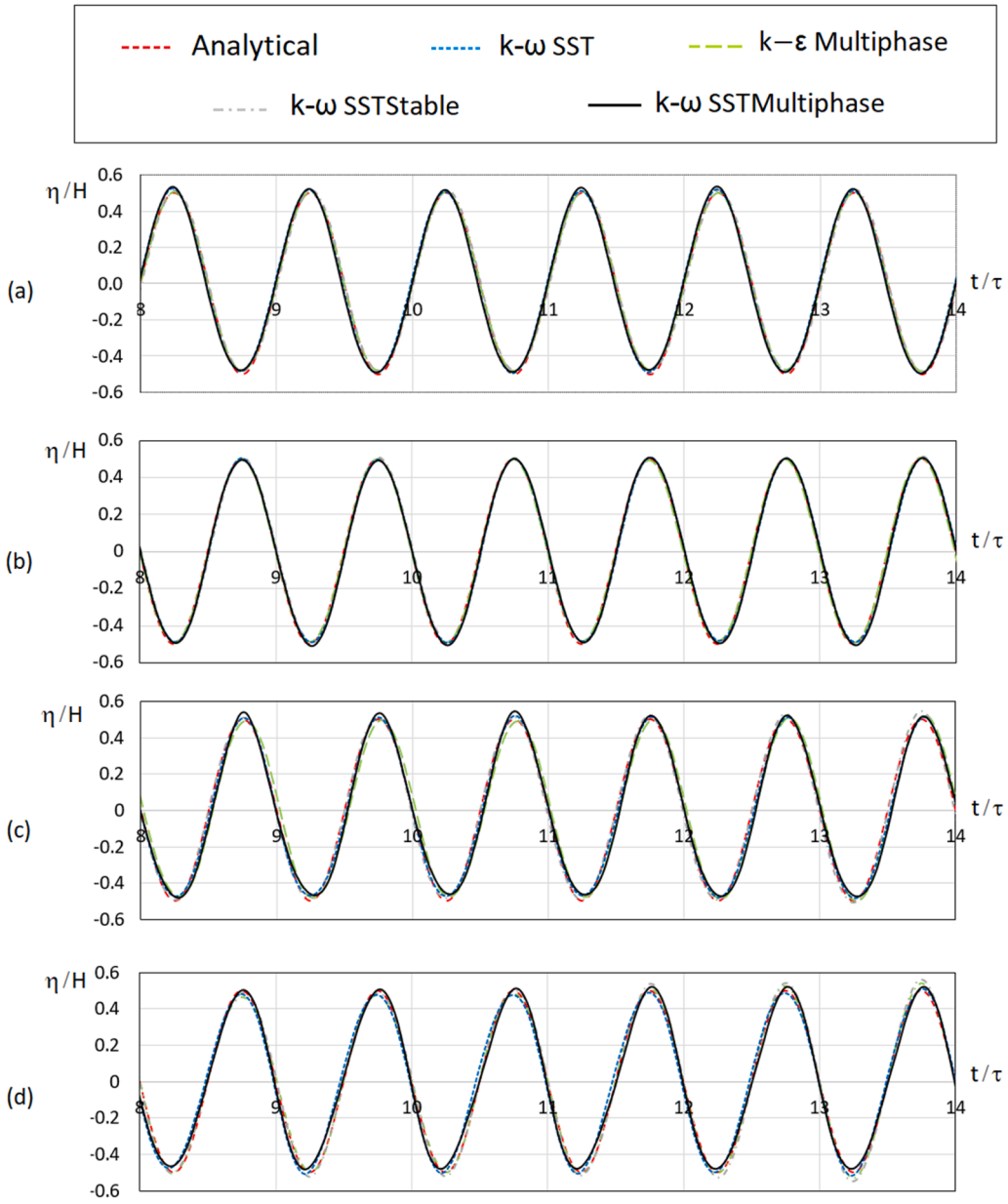


**Fig. 3.** Computed results using different turbulent models and comparison with analytical solution using applied linear wave at (a) $\boldsymbol{x} = 0.5\boldsymbol{L}$, (b) $\boldsymbol{x} = 1\boldsymbol{L}$, (c) $\boldsymbol{x} = 2\boldsymbol{L}$, (d) $\boldsymbol{x} = 3\boldsymbol{L}$.

**Table 5**
Specifications of the applied non-linear wave.

| Period $\tau$ ($s$) | Wave amplitude $H$ ($m$) | Water depth $h$ ($m$) | Wave number $k$ ($m^{-1}$) | Wavelength $L$ ($m$) |
|---|---|---|---|---|
| 2.2 | 0.04 | 0.4 | 1.5259 | 4.1156 |

**Table 6**
Mesh dependency study for non-linear Stokes II wave theory simulations.

| Mesh | Number of cells | Smallest cell size ($m^2$) | RMSE (-) |
|---|---|---|---|
| Very coarse | $86 \times 10^3$ | $0.02 \times 0.01$ | 0.017063 |
| Coarse | $142 \times 10^3$ | $0.015 \times 0.007$ | 0.011201 |
| Fine | $192 \times 10^3$ | $0.012 \times 0.006$ | 0.008477 |
| Very fine | $267 \times 10^3$ | $0.01 \times 0.005$ | 0.008362 |

computational domain, 30 $m$ long and 1 $m$ height is employed, and finer grid cells are considered near the free-surface interface area. A mesh dependency study similar to what was conducted for linear wave theory test case is performed as shown in Table 6 using k-ω SST-multiphase turbulence model with four different mesh resolutions, and very fine mesh with approximately $267 \times 10^3$ grid cells was chosen for the rest of the simulations. The results were compared with analytical solution for the surface elevation displacement at 4 different distances from the inlet (i.e. $x = 0.5L, 1L, 2L, 3L$), as shown in Fig. 4. Analogously, for linear waves, good agreement between computational fluid dynamics and analytical results are observed, while with progression in time and distance from the wave generator boundary, a small deviation from the analytical solution could be distinguished. The results in Fig. 4d demonstrate that simulating flow using turbulent models k-ω SST-stable and K-ω SST-multiphase offer better prediction of the non-linear Stokes II model.

### 3.1.3. *Generation and propagation of the irregular wave*

An irregular wave is constructed by linear superposition of regular wave components [44]. Here, for the purpose of the validation of the numerical model for an irregular wave, generation of an irregular wave was done using linear superposition of a group of four regular linear

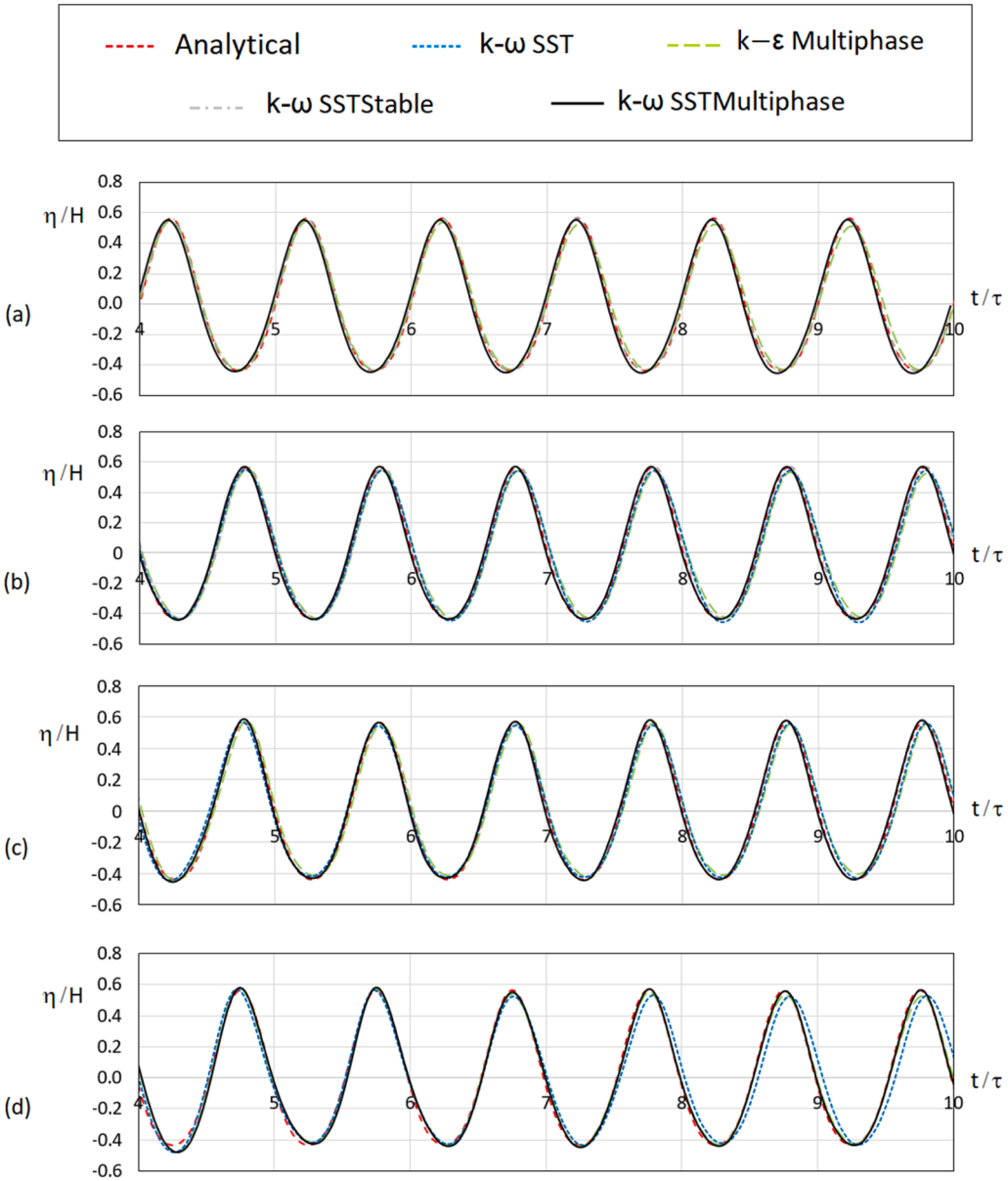


**Fig. 4.** Simulation results using different turbulent models and analytical solution for the applied non-linear wave at (a) $x = 0.5L$, (b) $x = 1L$, (c) $x = 2L$, (d) $x = 3L$.

**Table 7**
specifications of the applied linear waves for generation of an irregular wave.

| Waves | Period τ (*s*) | Wave amplitude *H* (*m*) | Water depth *L* (*m*) | Wave number *k* ($m^{-1}$) |
|---|---|---|---|---|
| No.1 | 1.8 | 0.02 | 1 | 1.4011 |
| No.2 | 0.95 | 0.008 | 1 | 4.4557 |
| No.3 | 1.3 | 0.01 | 1 | 2.417 |
| No.4 | 2.5 | 0.03 | 1 | 0.8988 |

waves with different wave phase shift as listed in Table 7 and presented in Fig. 5a.

A same computational domain as used in the regular linear wave test was deployed. The simulation results of wave surface elevation at $x = 3$ *m* away from the inlet was compared with the analytical solution as shown in Fig. 5b. The computed results confirm the high capability of the numerical model in simulating irregular waves; however, some discrepancy with analytical findings observed in the use of different turbulence closure models. The results of k-ω SST-stable and k-ω SST-multiphase turbulent models are quite similar and also close to the analytical solution, while k-ε multiphase and k-ω SST show some deviation from the analytical solution which grows in time.

### 3.1.4. *Wave flume with a submerged trapezoidal bar*

In this test case, the model is validated against the experimental data from Beji and Battjes [45] to evaluate interaction of regular waves with a submerged breakwater. Beji and Battjes [46], Beji and Battjes [45] conducted a series of experimental tests in a wave flume with a submerged trapezoid bar for regular and irregular waves. The test was

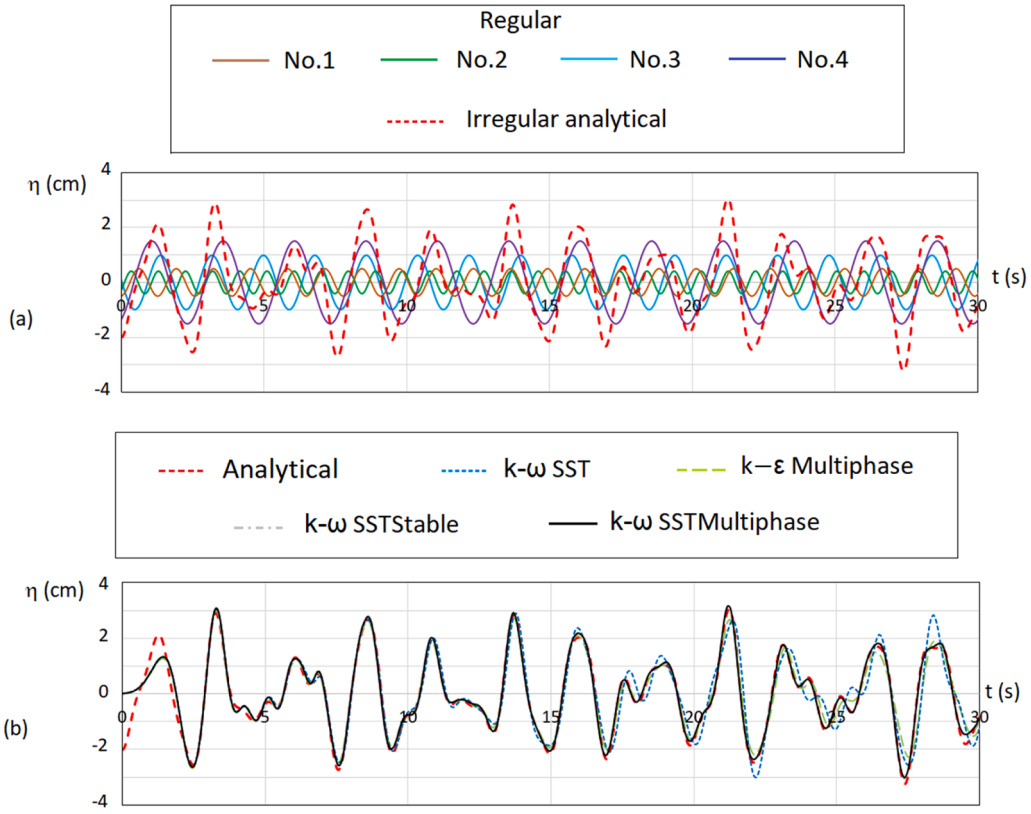


**Fig. 5.** (a) Applied linear waves to generate an irregular wave, (b) simulation results using different turbulent models and analytical solution for the applied irregular wave at $x = 3$ *m* from the wave generator boundary.

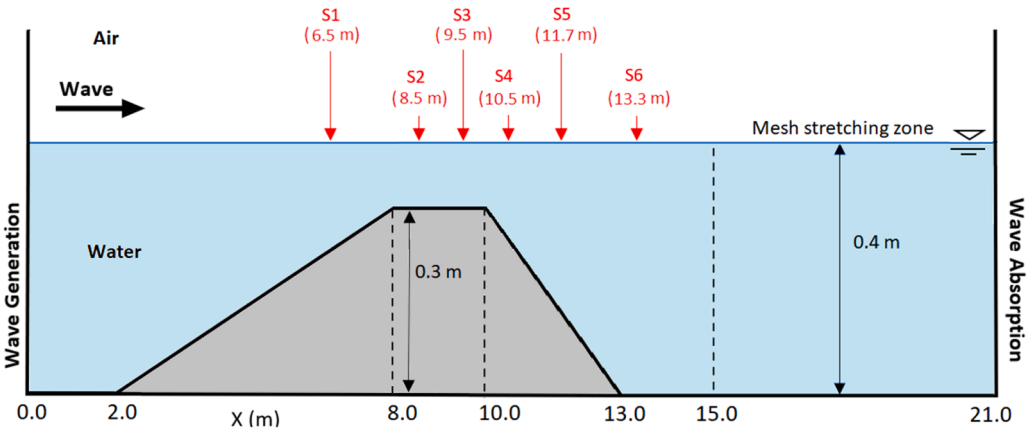


**Fig. 6.** Schematic of the generated computational domain for wave flume test with submerged trapezoid bar following Beji and Battjes [45].

**Table 8**
Generated mesh for mesh dependency study for wave flume with a submerged trapezoid bar test case.

| Mesh | Number of cells | Smallest cell size ($m^2$) | RMSE (-) |
|---|---|---|---|
| Coarse | $215 \times 10^3$ | $0.01 \times 0.003$ | 0.05632 |
| Medium | $320 \times 10^3$ | $0.007 \times 0.002$ | 0.04989 |
| Fine | $410 \times 10^3$ | $0.005 \times 0.0013$ | 0.04734 |

conducted in a flume with dimension 37.7 m long, 0.8 wide, and 0.75 m deep. The entire set of experiments were done using still water at a level of 0.4 m. The toe of the trapezoid bar was located at 6 m from the wave-generation board, while a beach with a 1:25 slope was constructed at the other end of the flume to serve as a wave absorber. Additional details of the experiment can be found in Beji and Battjes [46].

Of particular relevance for this study is the experiment performed in Beji and Battjes [45], where the tests was run using periodic incident

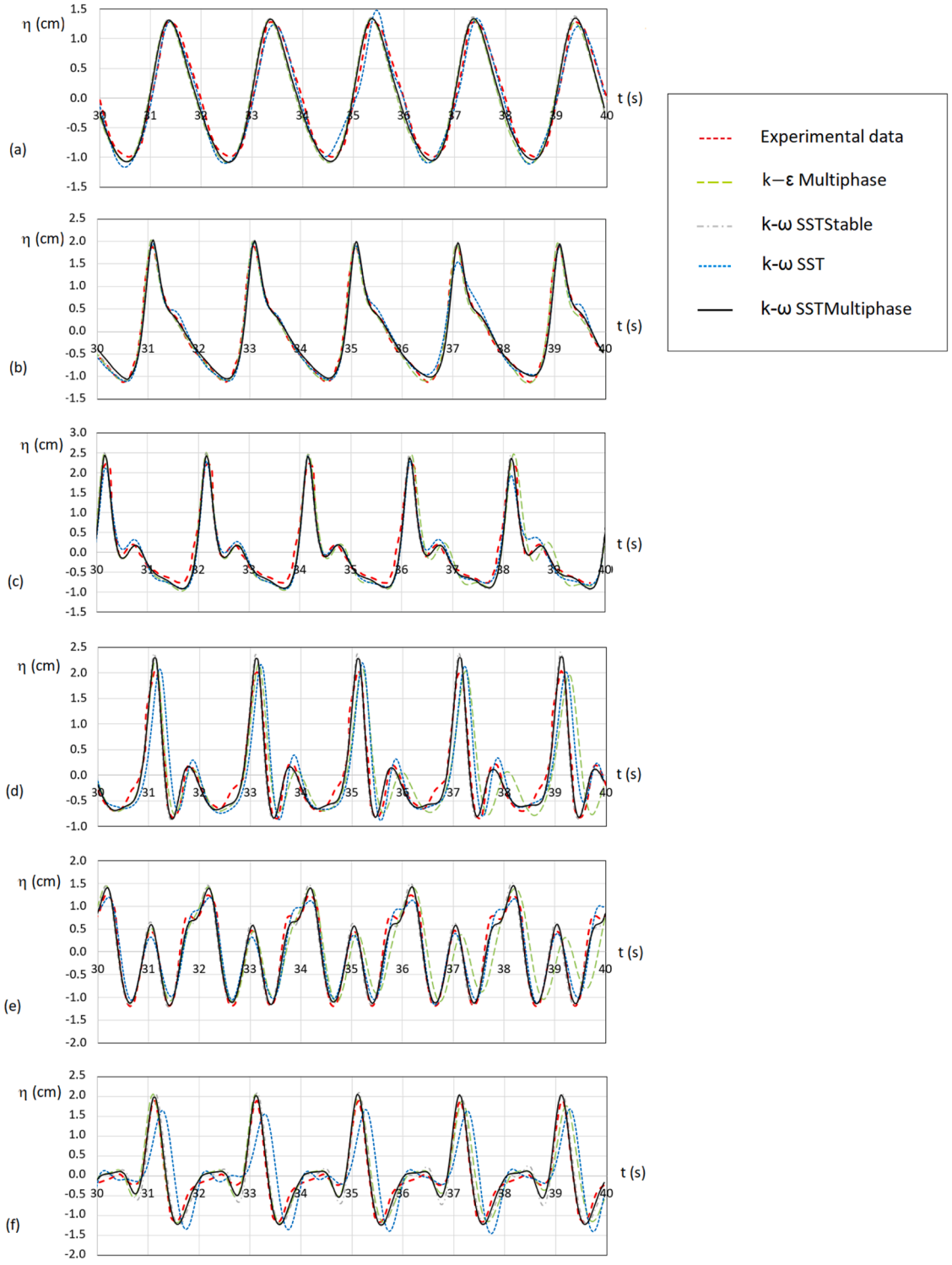


**Fig. 7.** Computed results using different turbulent models and experimental result by Beji and Battjes [45] for wave flume test with submerged trapezoid bar at (a) S1, (b) S2, (c) S3, (d) S4, (e) S5, (f) S6.

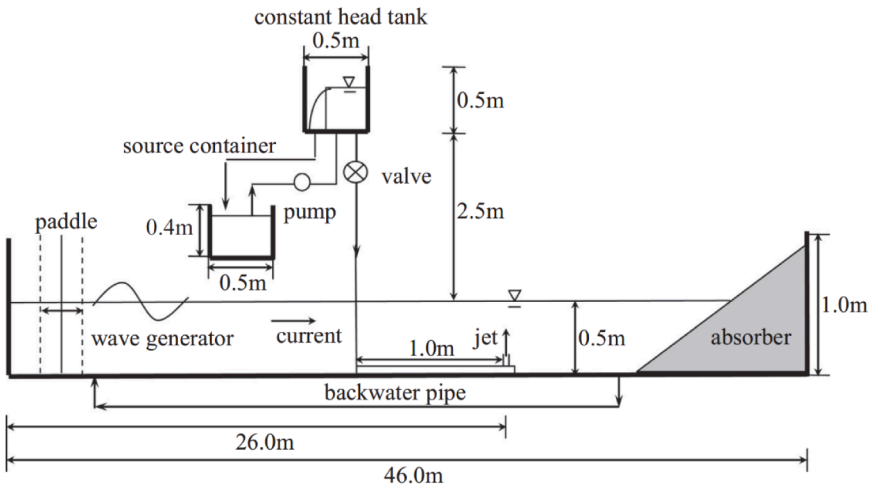


**Fig. 8.** Schematic of experimental setup by Xu et al. [17].

nonbreaking waves with period of $\tau = 2 \quad s$ and wave height of $H = 0.02 \quad m$. Surface elevation changes at 6 different stations above and downstream of the breakwater for 10 s were reported.

To reproduce the above experiment using the developed model, a numerical setup for the test included a two-dimensional computational domain 21 $m$ long and 1 $m$ high were generated as shown in Fig. 6. Following a similar configuration to the experimental flume of Beji and Battjes [45], the breakwater toe is placed 2 m from the wave generator boundary, while the beach located at the end of the flume is replaced with a wave absorption boundary. A cell stretching wave damping technique, as suggested by Mohseni and Soares [30], is considered in last 6 $m$ of the mesh to ensure wave reflections are suppressed. A second-order regular wave was generated at the wave generator boundary and propagated towards the trapezoid-bar. An initial mesh

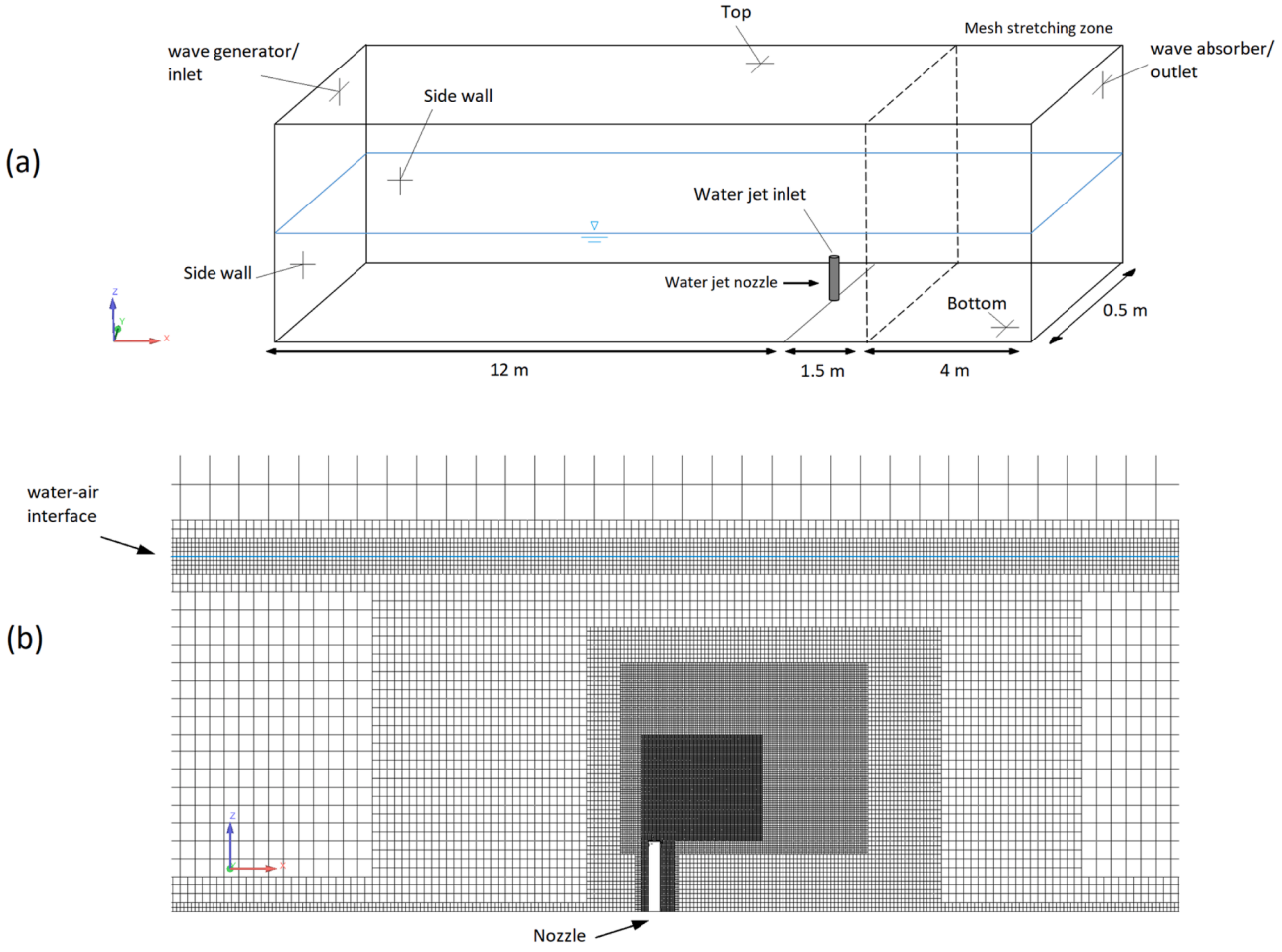


**Fig. 9.** (a) Schematic of the computational domain; and (b) Zoomed in section of the generated mesh in the ***x-z*** plane around the non-buoyant jet under current-only and current-wave environments.

**Table 9**
Generated mesh for mesh dependency study for non-buoyant jet under current-only and wave-current environments case.

| Mesh | Number of cells | Background mesh cell size ($m^3$) | RMSE (-) |
|---|---|---|---|
| Coarse | $1.8 \times 10^6$ | $(0.06)^3$ | 0.04627 |
| Medium | $2.2 \times 10^6$ | $(0.055)^3$ | 0.03409 |
| Fine | $2.8 \times 10^6$ | $(0.05)^3$ | 0.03103 |

dependency study was carried out using meshes of different sizes as provided in Table 8. For each case, RMSE was calculated in comparison with experimental data for time evolution of the surface elevation in a specific point from the wave generator boundary. A mesh with around 0.41 million grid cells with the smallest grid cell size, 0.5 cm × 0.13 cm, distributed near the free-surface region along the whole domain was chosen.

Simulations with different turbulence models (i.e. k-ω SST, k-ω SST-stable, k-ω SST-multiphase, k-ε multiphase) are carried out over the duration of 40 s. The results shown in Fig. 7 presents a comparison between the results at the last 10 s of the simulations with the experiment performed by Beji and Battjes [45]. Overall, a good qualitative and quantitative agreement can be drawn between the results for all stations in terms of generation of the crest and trough, in particular those performed here using k-ω SST-multiphase shows the closest agreement with experimental data. Overall, the simulation results from Sections 3.1.1-3.1.4 disclosed that k-ω SST-multiphase can be used as a reliable turbulence model in simulation of different wave propagations. This can be justified by considering that this turbulence model is an enhanced multiphase version of original k-ω SST in OpenFOAM®,which has a proven capability in predicting adverse pressure gradient and separating flow [29].

### 3.1.5. *Non-buoyant jet under current-only and wave-current environments*

To evaluate the capability of the developed model in predicting flow field of a submerged jet under wave and current conditions, results of the empirical and numerical study that were carried out by Xu et al. [17] for modelling of three-dimensional flow structure of a non-buoyant jet under current-only and wave-current conditions were considered. The experiments were performed in a flume that was 46 *m* long, 0.5 *m* wide, and 1.0 *m* deep. The static water depth in the experiments were kept at 0.5 *m*, and their test ran using currents with mean velocity of $u_c = 0.066$ *m/s*, waves with a period of $\tau = 1.4$ *s* with a height of $H = 0.03$ *m*. A vertical water jet with mean velocity of $u_{jet} = 0.5$ *m/s* was discharged from a round pipe with an inner diameter of, $d = 0.01$ *m*, located at the centre of the flume with the jet orifice positioned 0.1 *m* above the bottom bed. The schematic of the experimental setup is shown in Fig. 8. In Xu et al. [17], a numerical solution was computed using a three-dimensional Large Eddy Simulation (LES) model. The experimental and numerical results were compared in terms of vertical profile of mean velocity at eight downstream locations.

The capability and accuracy of the presently developed solver is measured against the experiment of Xu et al. [17] to accurately predict the flow of non-buoyant jet under both current-only and wave-current conditions. For this purpose, a three-dimensional computational domain with 17.5 *m* long, 0.5 *m* wide, and 1.0 *m* deep is considered, where the vertical pipe jet is located at the symmetry plane and 12 *m* from the inlet boundary condition as shown in Fig. 9a. The mesh is generated using the snappyHexMesh technique and a mesh dependency study is performed for three different mesh sizes as reported in Table 9. RMSE is calculated in comparison with experimental data which indicates a high level of mesh independence for medium and fine meshes. A computational domain with approximately 2.8 million mesh cells is selected for the rest of the study. Fig. 9b shows part of the generated mesh around the area of the interest near the vertical pipe in the *x-z* plane. A cell stretching wave damping technique was used in last 4 *m* of the right of the domain to ensure wave reflections are suppressed. Findings from Sections 3.1.1-3.1.4 informed the use of k-ω SST-multiphase and therefore is chosen as the turbulence closure model.

To be able to track the plume of the water jet, an advection-diffusion equation for concentration, *C*, was passively solved alongside of the flow field equations, given by the following,

$$\frac{\partial \rho C}{\partial t} + \nabla.[\rho \boldsymbol{u} C] = \nabla.[D \nabla C], \tag{18}$$

where $D$ is the diffusion coefficient and is defined by $\mu + \mu_t$.

The applied boundary conditions for the setup is defined in Table 10, which is similar to the one defined for two-dimensional test cases (Table 2) with additional terms to account for water jet inlet boundary and concentration, *C*. The transverse flow patterns associated with the presence of side walls are assumed to be negligible. Consequently, the side walls are treated using symmetry boundary conditions to reduce the required mesh refinement near the side walls which leads to a decrease in computational mesh required and accordingly reducing computational cost. To mimic the velocity profile at the vertical water jet inlet, a partially developed flow profile is set at the water jet inlet. This is obtained by conducting a preliminary simulation with a 0.1 *m* length hydraulically smooth pipe where a uniform velocity ($u_{jet} = 0.5$ *m/s*) was provided at the inlet of the pipe, and the outlet velocity profile is extracted. In the present version of olaFlow, the current flow at the inlet is defined using a uniform mean velocity. Therefore, the computational domain has to be chosen with an appropriate upstream length to ensure fully developed flow at the region of interest, close to the water jet discharge area. Furthermore, olaFlow is currently not capable of modelling the current-wave interaction, hence wave and current are generated independently (uncoupled). Interested readers are referred to Xu et al. [17] and Li and Herbich [47] for more information.

The results for the present model are compared against the numerical and experimental results of Xu et al. [17] for both current-only and current-wave coexisting environments, shown in Fig. 10 and Fig. 12, respectively. Xu et al. [17] reported the mean flow velocity profile at eight different downstream vertical lines located at $x/d = 0, 1, 2, 4, 7, 10, 14, 18$ on the symmetry plane ($y/d = 0$) in each case. A very good agreement between the results can be observed in terms of the flow

**Table 10**
Applied boundary conditions for non-buoyant jet under current-only and current-wave environment.

| Boundaries | Vertical water jet inlet | Side walls | Top (patch/atmospheric) | Bottom/ Pipe wall (no-slip wall) | Inlet (wave generator) | Outlet (wave absorber) |
|---|---|---|---|---|---|---|
| Velocity ($\boldsymbol{u}$) | fixedValue | Symmetry | pressureInletOutletVelocity | fixedValue | waveVelocity | waveAbsorbtion |
| Pressure ($p$) | zeroGradient | Symmetry | totalPressure | zeroGradient | zeroGradient | zeroGradient |
| Phase fraction ($\alpha$) | fixedValue | Symmetry | inletOutlet | zeroGradient | waveAlpha | zeroGradient |
| Turbulent kinetic energy ($k$) | fixedValue | Symmetry | inletOutlet | kqRWallFunction | fixedValue | inletOutlet |
| Turbulent dissipation ($\varepsilon$) | fixedValue | Symmetry | inletOutlet | epsilonWallFunction | fixedValue | inletOutlet |
| Specific turbulent dissipation rate($\omega$) | fixedValue | Symmetry | inletOutlet | omegaWallFunction | fixedValue | inletOutlet |
| Kinematic turbulent viscosity ($\nu_t = \mu_t/\rho$) | calculated | Symmetry | Calculated | nutkWallFunction | calculated | calculated |
| Concentration ($C$) | fixedValue ($C$=1) | Symmetry | inletOutlet | zeroGradient | fixedValue ($C$=0) | inletOutlet |

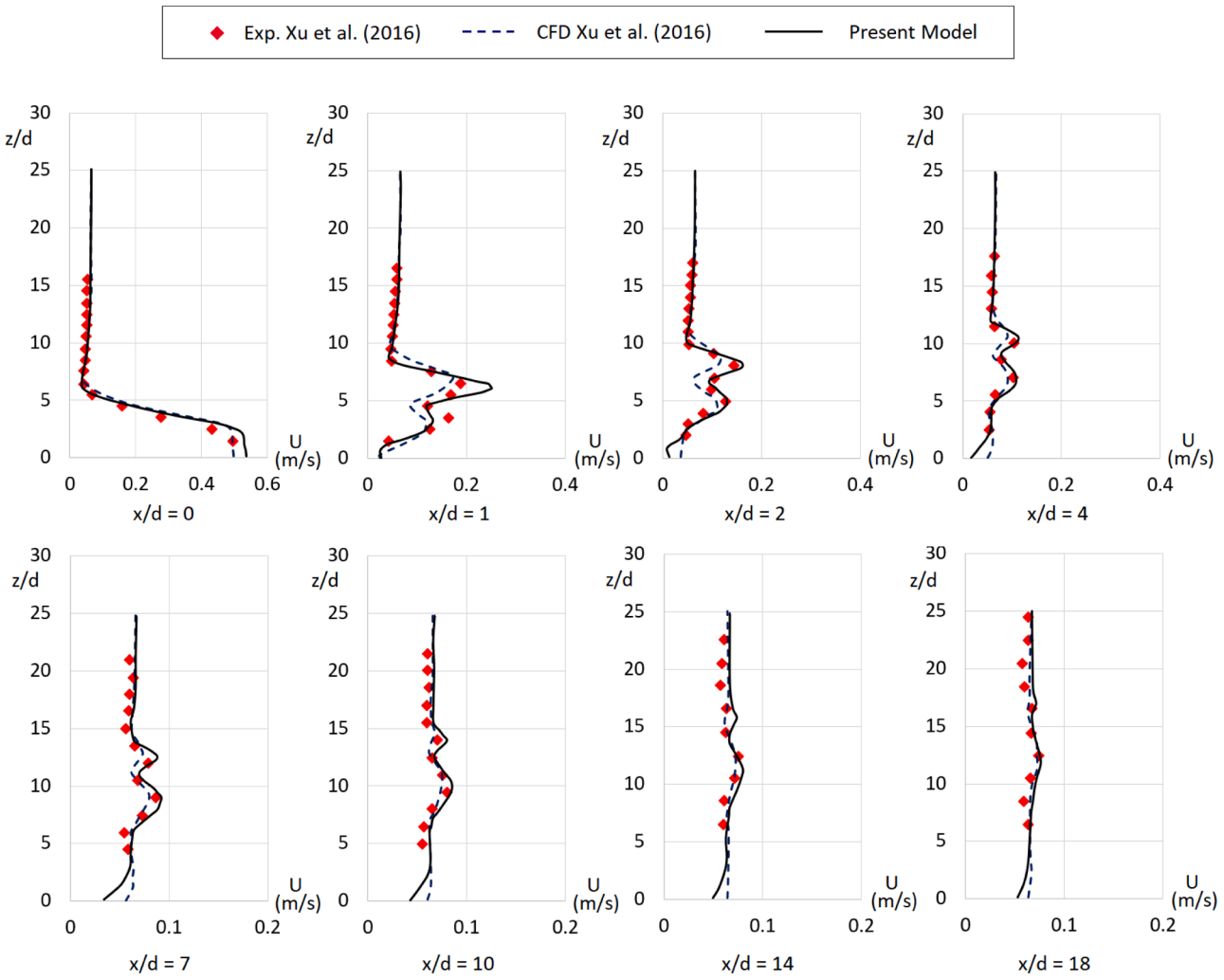


**Fig. 10.** Comparison of the mean flow velocity profile between experimental and numerical results at eight different downstream vertical lines located at $x/d = 0$, 1, 2, 4, 7, 10, 14, 18 on the symmetry plane under current-only condition.

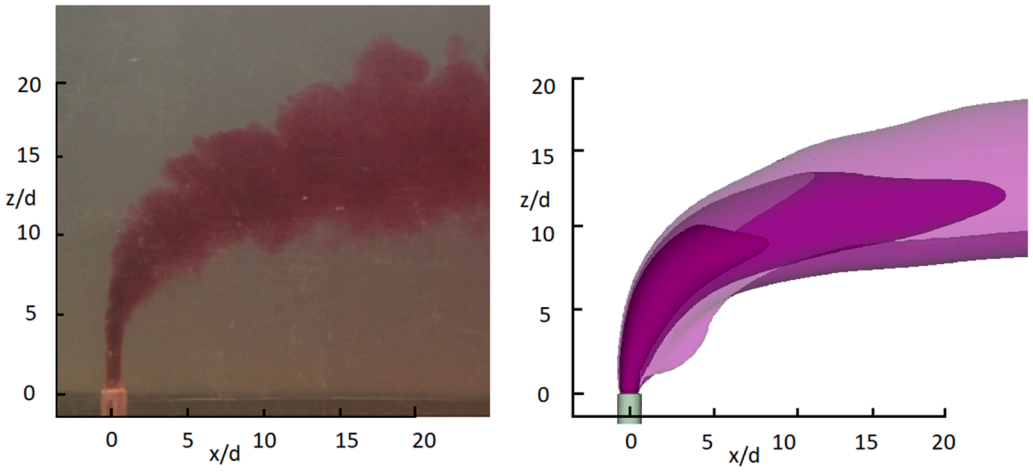


**Fig. 11.** Comparison of the instantaneous concentration profile between the experimental result of Xu et al. [17] and numerical results of the developed model under current-only condition.

profile pattern and magnitude of the flow velocity for each case. The results prove the capability and accuracy of the present developed model in predicting flow hydrodynamics of a submerged water jet under current-only and current-wave coexisting environments. Furthermore, the instantaneous flow pattern resulted from the injection of dye into the water jet in Xu et al. [17] are compared with isosurfaces of the instantaneous concentration profile of the present model, shown in Figs. 11 and 13 for current-only and current-wave conditions, respectively. Apart

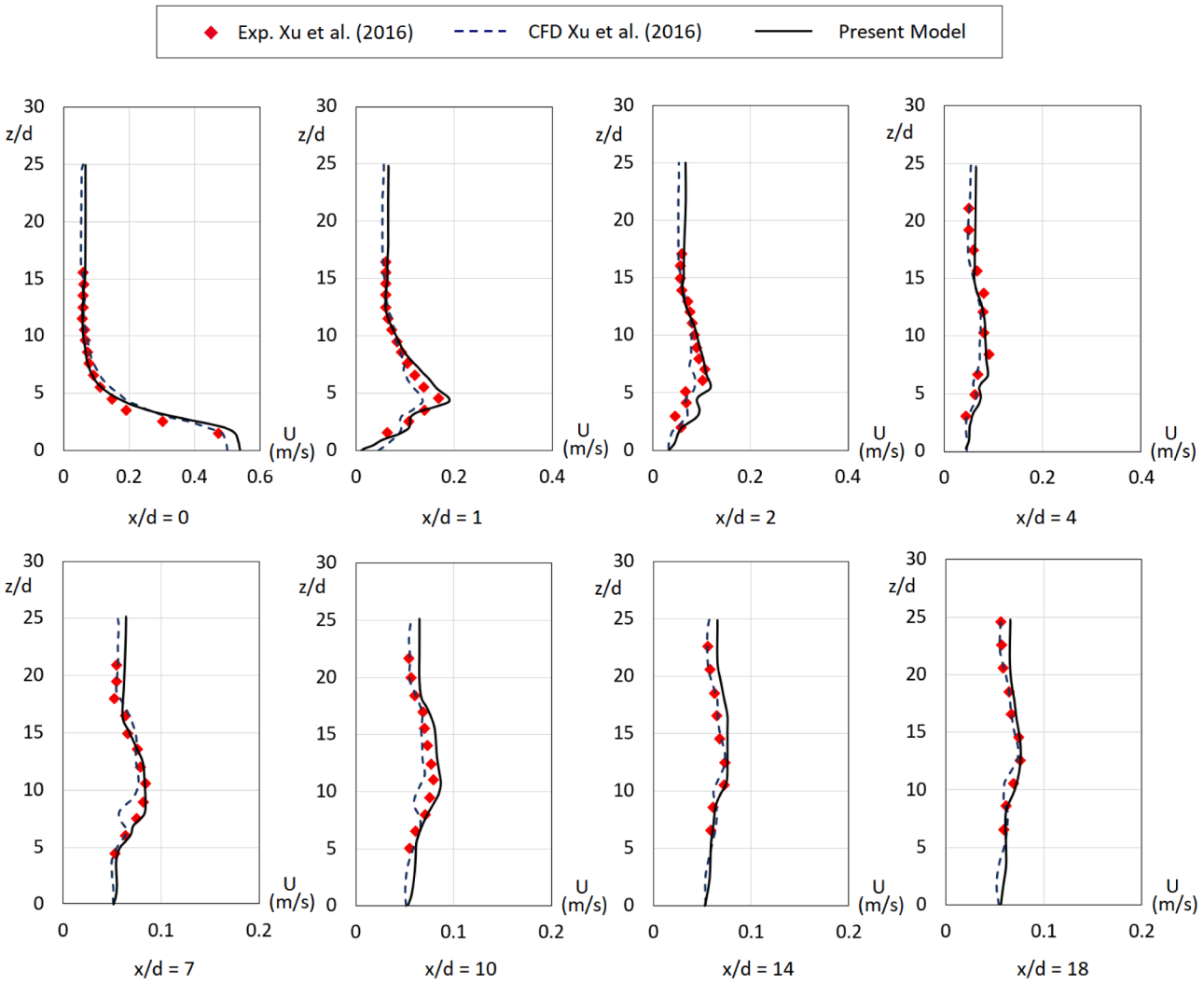


**Fig. 12.** Comparison of the mean flow velocity profile between experimental and numerical results at eight different downstream vertical lines located at $x/d = 0$, 1, 2, 4, 7, 10, 14, 18 on the symmetry plane ($y/d = 0$) under current-wave condition.

from the identified higher diffusion rate near the discharge outlet, the numerical model precisely estimated most of the flow characteristics in terms of shape, height, and location of the mixing jet in both current-only and current-wave environments.

### 3.2. Hydro-Thermal modelling

In the following, the robustness of the coupled hydro-thermal algorithm is assessed by validating the model against different thermal-induced buoyant submerged jet experiments. For this purpose, the results of a series of tests for thermal-induced buoyant submerged horizontal jets in stationary water are considered, followed by an ultimate experimental test conducted at the coastal laboratory of the University of Plymouth for an inclined thermal-induced buoyant water jet operating under both current-wave coexisting environments.

#### 3.2.1. Horizontal buoyant jet in stagnant shallow water

To validate the hydro-thermal model, experimental data conducted by Sobey et al. [48] for a horizontal round buoyant jet in stagnant shallow water was adopted. The experiment took place in a 3 $m$ × 3 $m$ square tank with a depth of 0.35 $m$. A horizontal hot water jet inlet with a diameter, $D_0$= 27.5 $mm$, was positioned at the horizontal centreline at one end of the tank, as shown in Fig. 14. The buoyancy parameter, $(\rho_w - \rho)/\rho_w$, was held constant at nominally 0.003, where $\rho$ and $\rho_w$ represents the density of the jet and tank water, respectively.

A total of 75 tests were conducted with variation in water depth and different, jet depth and speed. In all tests, the Reynolds number was sufficiently high ($Re \geq 3900$) to ensure turbulent flow. Temperature fields in vertical planes through the jet were measured at 8 different locations, at $x$ = 60, 100, 200, 270, 360, 400, 500, and 570 $mm$. The measurements were performed when a reasonably close approximation to a steady flow situation was established.

The results were categorized based on the range of free surface parameter, $(H - Z_0)/l_M$, where $H$ was water depth, $Z_0$ was jet inlet height from the bed, and $l_M$ was length scale parameter. Source momentum and buoyancy fluxes were assumed to be the dominant parameters [48], therefore $l_M$ was calculated using,

$$l_M = \left(\frac{\pi}{4}\right)^{0.25} D_0 \, Fr \tag{19}$$

where $Fr$ is the source densimetric Froude number,

$$Fr = \frac{V_0}{\left(g_0' D_0\right)^{0.5}} \tag{20}$$

and $V_0$ is the water source jet velocity, and $g_0'$ is defined as,

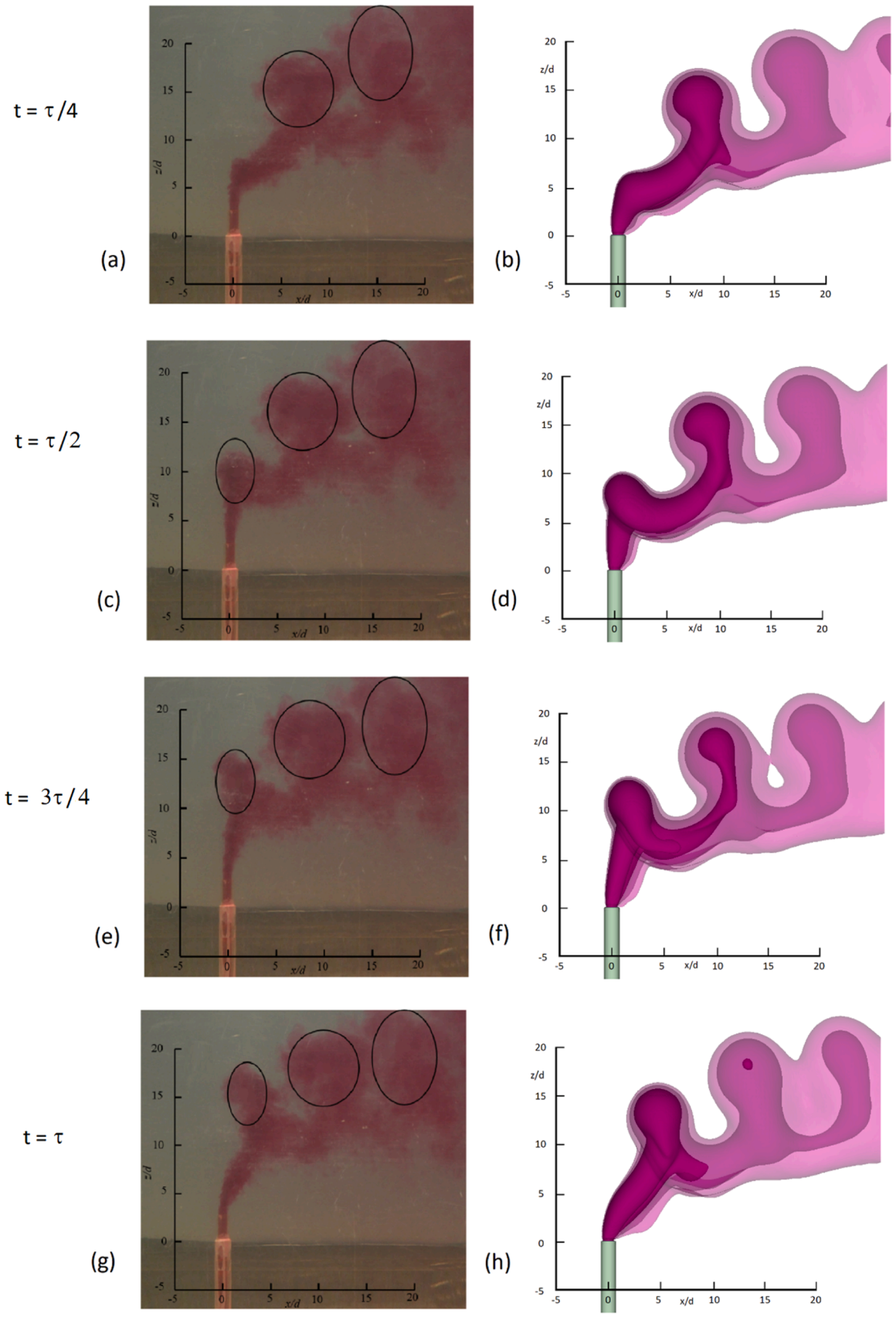


**Fig. 13.** Comparison of the instantaneous concentration profile between the experimental result of Xu et al. [17] and numerical results of the developed model under current-wave coexisting condition at different time period of the wave: (a, b) $t = \tau/4$, (c, d) $t = \tau/2$, (e, f) $t = 3\tau/4$, (g, h) $t = \tau$.

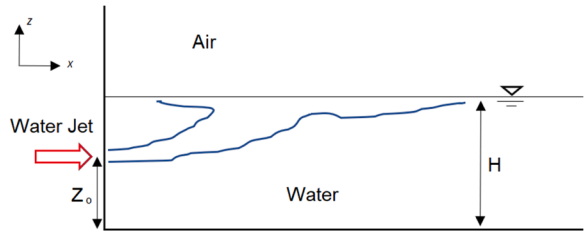


**Fig. 14.** Schematic of the horizontal buoyant jet in stagnant shallow water by Sobey et al. [48].

$$g_0' = \frac{(\rho_w - \rho)g}{\rho} \tag{21}$$

with $g$ denoting the gravitational acceleration.

Sobey et al. [48] reported results on four categories. Three tests from each category were selected for numerical modelling are listed in Table 11. The chosen tests represent a wide spectrum of free surface parameter within each category.

The dispersion models were conducted in a three-dimensional computational domain with dimensions of 3 $m$ length, 1.5 $m$ width, and 0.4 $m$ depth as depicted in Fig. 16. A vertical symmetry plane was applied at the centreline, where water jet inlet was located at $x = 0$ to reduce the numerical burden and computational time. The computational domain was discretized using unstructured hexahedral grids.

A mesh dependency study was performed for the cases, and the results of the centreline path of the jet for test No.36 from Table 11 for three different mesh sizes were presented in Fig. 15. The results revealed that mesh resolution was sufficient for all meshes as no significant differences were observed. A computational domain with roughly 1.3 million mesh cells was chosen for the simulations in each case.

To maintain a similar state to the experiments for buoyancy parameter, the jet and tank water temperature of 294 $K$ and 305 $K$ was specified, respectively, providing a small density variation $(\rho_w - \rho)/\rho_w \approx 0.003$.

The applied boundary conditions for the computational domain, which also includes boundaries for temperature field for hydro-thermal modelling, are reported in Table 12. A fully developed flow profile was provided at the water jet inlet. This was done by conducting a preliminary test with a 1 $m$ length pipe where a constant velocity was provided at the inlet of the pipe, calculated based on the provided flow rate in each test, to yield fully developed flow at the outlet.

To ensure that a fully developed flow jet was achieved in each case, simulated results were compared over time. It was realized that simulation time of 40 $s$ was sufficiently long enough to enable fully developed flow to be attained, as no substantial changes in water jet behaviour could be observed thereafter.

In the pertinent literature, Huai et al. [49] and Kheirkhah Gildeh et al. [50], Kheirkhah Gildeh et al. [51] conducted numerical modelling of turbulent buoyant jets in stationary ambient water. These studies applied RANS combined with different turbulence closure models. In result, the linear eddy viscosity model, realizable k−$\varepsilon$ turbulence model, Reynolds Stress Models, and LRR, were claimed to be the most reliable and accurate in modelling of Coanda effect, buoyant and non-buoyant jet in stagnant environment. In the present study, to evaluate the performance of the applied turbulence model (i.e. k-ω SST-multiphase) in discharge dispersion modelling, similar simulations using the realizable

**Table 11**
Test categories by Sobey et al. [48] and chosen tests for simulation from each category.

| Category Number | Categories range | No. test in the category | Sim. test number | $H$ $(m)$ | $Z_0$ $(m)$ | $l_M(m)$ | Flow rate $(l/s)$ | $\frac{(H-Z_0)}{l_M}(-)$ |
|---|---|---|---|---|---|---|---|---|
| 1 | $0.075 \le (H - Z_0)/l_M \le 0.1$ | 5 | **03** | 0.3 | 0.278 | 0.241 | 0.169 | 0.0911 |
| | | | **58** | 0.1 | 0.075 | 0.266 | 0.173 | 0.0939 |
| | | | **59** | 0.1 | 0.075 | 0.327 | 0.212 | 0.0764 |
| 2 | $0.125 \le (H - Z_0)/l_M \le 0.15$ | 3 | **35** | 0.2 | 0.15 | 0.385 | 0.254 | 0.1298 |
| | | | **57** | 0.1 | 0.075 | 0.191 | 0.125 | 0.1305 |
| | | | **65** | 0.1 | 0.05 | 0.393 | 0.254 | 0.1273 |
| 3 | $0.3 \le (H - Z_0)/l_M \le 0.4$ | 8 | **38** | 0.2 | 0.1 | 0.259 | 0.172 | 0.3855 |
| | | | **45** | 0.2 | 0.05 | 0.382 | 0.252 | 0.3923 |
| | | | **61** | 0.1 | 0.05 | 0.135 | 0.088 | 0.3714 |
| 4 | $0.5 \le (H - Z_0)/l_M \le 1.0$ | 16 | **36** | 0.2 | 0.1 | 0.128 | 0.083 | 0.5185 |
| | | | **37** | 0.2 | 0.1 | 0.193 | 0.127 | 0.5906 |
| | | | **43** | 0.2 | 0.05 | 0.254 | 0.170 | 0.7835 |

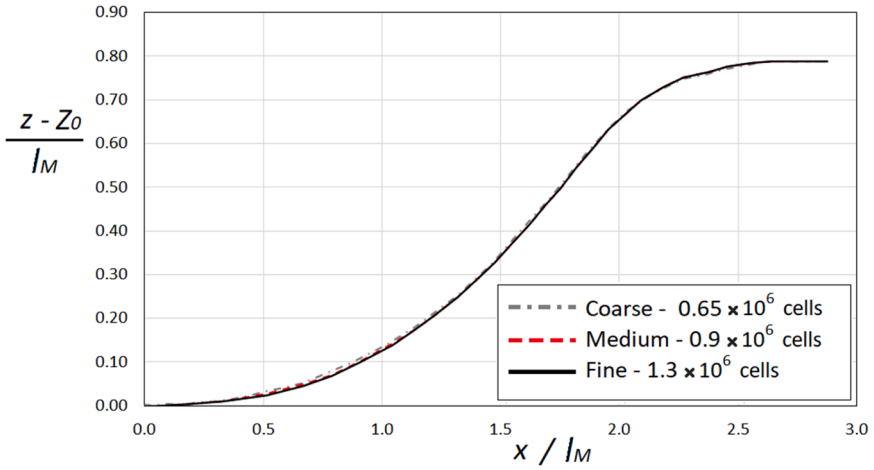


**Fig. 15.** Centreline path of the jet of the three generated meshes for horizontal buoyant jet in stagnant shallow water case for test No.36.

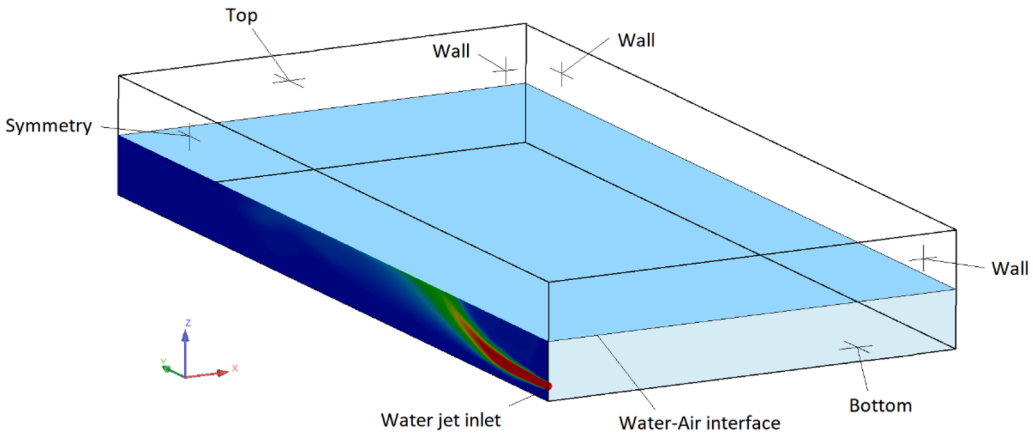


**Fig. 16.** Computational domain for hydro-thermal modelling of horizontal buoyant jet in the stagnant shallow water case.

**Table 12**
Applied boundary condition for hydro-thermal modelling of horizontal buoyant jet in the stagnant shallow water case.

| Boundaries | Water jet inlet | Symmetry | Top (patch/atmospheric) | Bottom/Wall (no-slip wall) |
|---|---|---|---|---|
| Velocity ($\boldsymbol{u}$) | fixedValue | Symmetry | pressureInletOutletVelocity | fixedValue |
| Pressure ($p$) | zeroGradient | Symmetry | totalPressure | zeroGradient |
| Phase fraction ($\alpha$) | fixedValue | Symmetry | inletOutlet | zeroGradient |
| Turbulent kinetic energy ($k$) | fixedValue | Symmetry | inletOutlet | kqRWallFunction |
| Specific turbulent dissipation rate($\omega$) | fixedValue | Symmetry | inletOutlet | omegaWallFunction |
| Turbulent dissipation ($\varepsilon$) | fixedValue | Symmetry | inletOutlet | epsilonWallFunction |
| Kinematic turbulent viscosity ($\nu_t = \mu_t/\rho$) | Calculated | Symmetry | Calculated | nutkWallFunction |
| Temperature ($T$) | fixedValue | Symmetry | inletOutlet | zeroGradient |

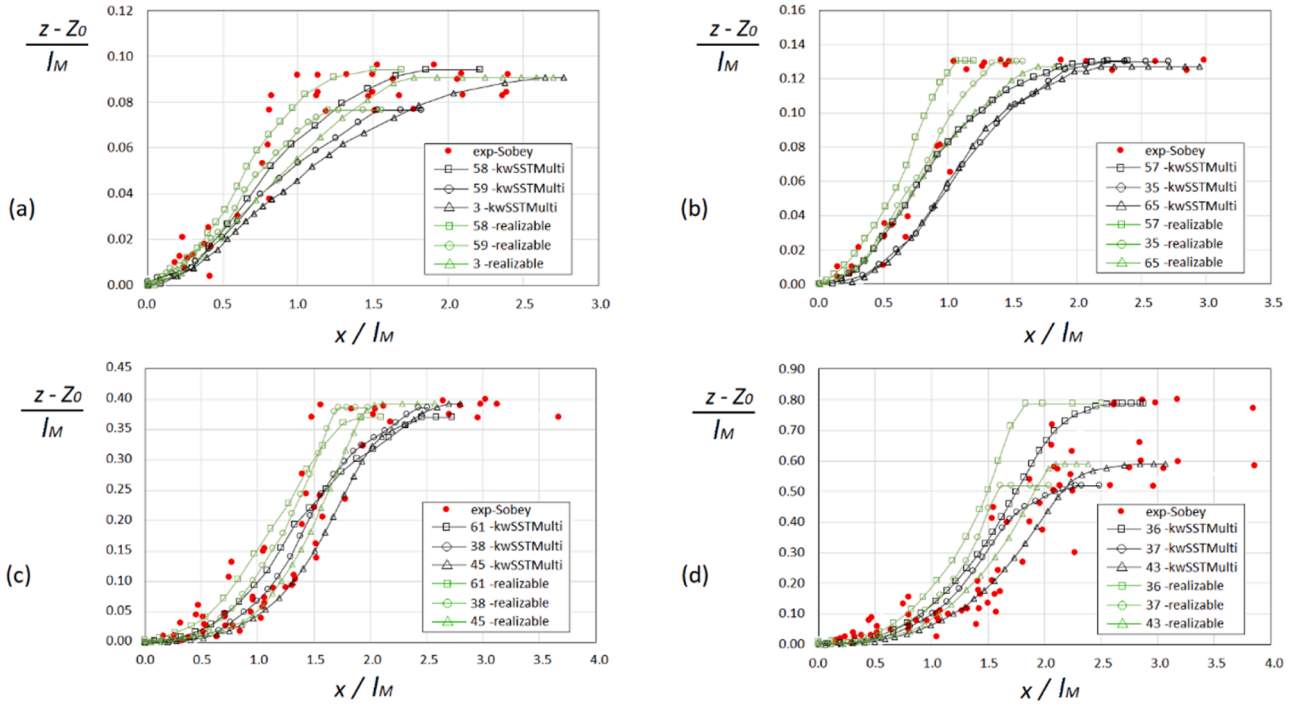


**Fig. 17.** Simulation results for the centreline path using k-ω SST-multiphase and realizable k−ε turbulence models, along with measurement data by Sobey et al. [48] for categories: (a) No.1, (b) No.2, (c) No.3, and (d) No.4.

k−$\varepsilon$ turbulence model were performed.

Fig. 17 illustrates the simulations and experimental data for the centreline path of the jet for the tests in each category. The root mean squared error (RMSE) was used to quantify the deviation of the simulation outcomes from the experimental data as shown in Table 13. The RMSE in each category represents the average computed RMSE for each case. To calculate the residuals of the simulation results and the experimental data, a nonlinear asymmetrical sigmoidal curve was fitted to each result.

The findings indicated that simulations with realizable k−ε showed

**Table 13**
RMSE of the simulations with k-ω SST-multiphase and realizable k−ε turbulence models with the experimental data.

| categories | No.1 | | No.2 | | No.3 | | No.4 | |
|---|---|---|---|---|---|---|---|---|
| Turbulence model | Real. k−ε | k-ω SST-Multi | Real. k−ε | k-ω SST-Multi. | Real. k−ε | k-ω SST-Multi | Real. k−ε | k-ω SST-Multi |
| Ave. RMSE | 0.01275 | 0.01624 | 0.01688 | 0.02330 | 0.0780 | 0.0681 | 0.2041 | 0.1480 |

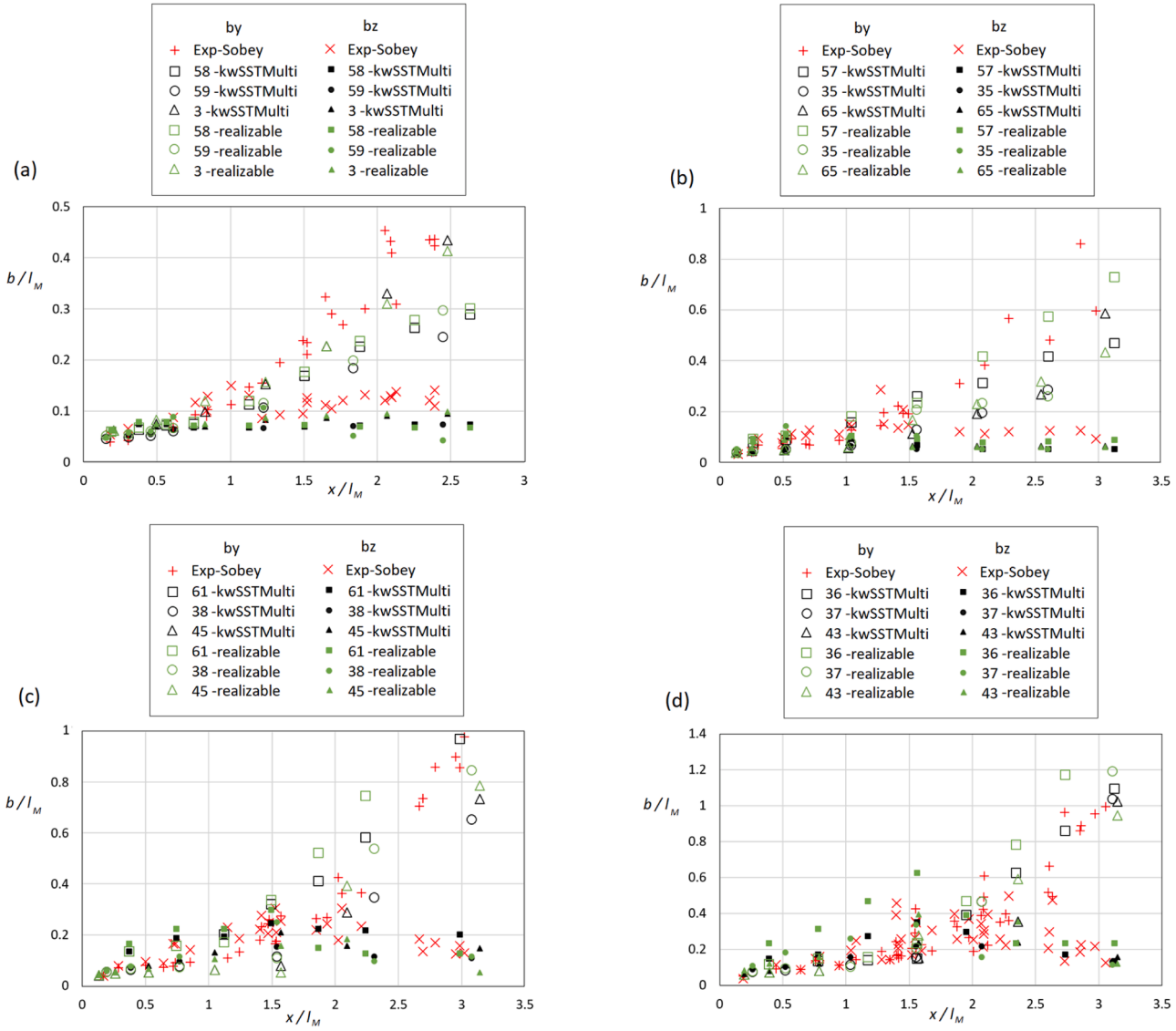


**Fig. 18.** Simulation results for horizontal, $b_x$, and vertical, $b_z$, half-widths of the water jet using k-ω SST-multiphase and realizable k−ε turbulence models, along with measurement data by Sobey et al. [48] for categories: (a) No.1, (b) No.2, (c) No.3, and (d) No.4.

better agreement with experimental data for cases with a small free surface parameter, such as category No.1 and No.2. With an increase in the free surface parameter, e.g., in categories No.3 and No.4, k-ω SST-multiphase demonstrated better consistency with the laboratory measurement data. Overall, k-ω SST-multiphase provided the most promising results in the hydro-thermal modelling of buoyant jet.

Fig. 18 showed the experimental and simulation results for the horizontal, $b_x$, and vertical, $b_z$, half-widths of the water jet for the tests. The measurement of half-widths indicates the capability of numerical models in simulating dispersion rates compared to experimental data. A small discrepancy can be observed between simulations and experimental data in the first two categories (i.e., No.1 & No.2), while the results for categories No.3 and No.4 agree very well with one another. Overall, the k-ω SST-multiphase model demonstrates strong potential in accurately modelling the experimental data conducted by Sobey et al. [48] and is therefore employed in subsequent simulations.

### 3.2.2. *Inclined buoyant hot-water jet under current-wave environment*

To evaluate the performance of the developed hydro-thermal model in a shallow-water coastal environment, an ultimate test was designed involving the discharge of a submerged hot water jet under current-wave coexisting conditions. The test configuration, primarily inspired by the work of Xu et al. [17], as shown in Fig. 8, utilised supplier tanks equipped with heaters to provide a hot water jet. An experimental test was designed and conducted in a 20 *m* long, 0.6 *m* wide and 0.8 *m* deep flume in the coastal laboratory of the University of Plymouth, that is capable of generating a combination of current and linear waves.

A round nozzle with a 45° inclined angle towards the end of the

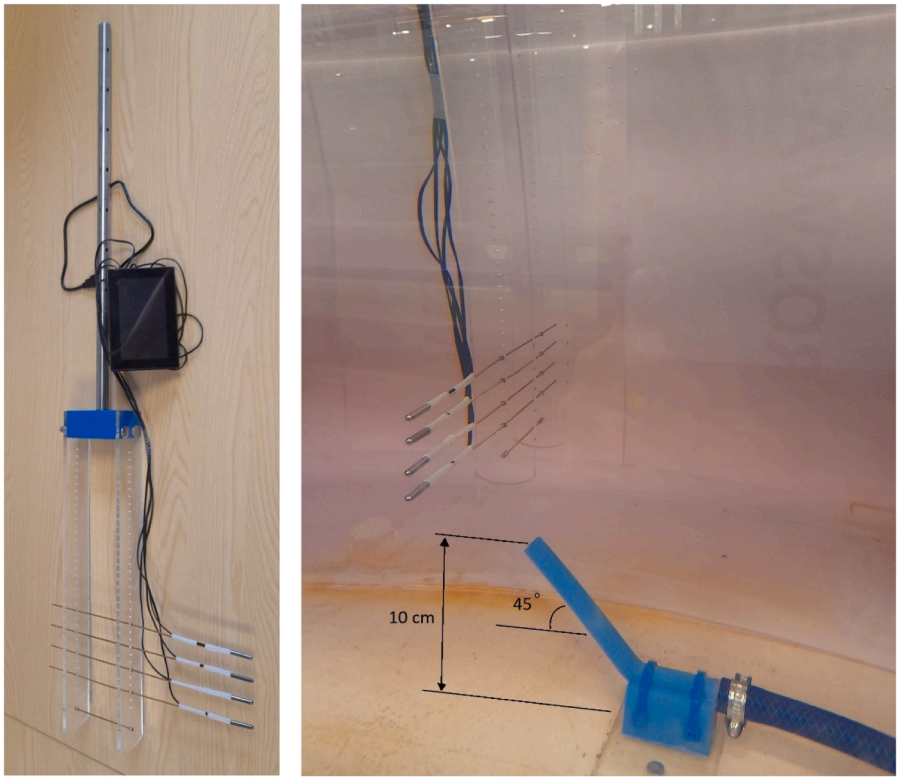


**Fig. 19.** (a) Designed setup for temperature measurement, (b) Positioning of the probes downstream of the nozzle outlet.

flume with an inner diameter of $d = 0.9$ *cm* was fixed at the bed and on the symmetry plane at 9 *m* from the start of the flume. The nozzle outlet was located 10 *cm* above the bed level and the water jet's mean velocity was set to 0.5 *m/s*. The static water depth in the experiment was maintained at 0.4 *m*, and the test ran under a current with a mean velocity of $u_c = 0.045$ *m/s* and a wave with a period of $\tau = 2$ *s* and a wave height of $H = 0.014$ *m*. Food colouring was injected into the supplier tanks to monitor the hot water jet's instantaneous flow pattern. The impact of the food colouring concentration on water density was considered negligible.

Throughout the experiment, the flume water temperature was maintained at 18 °C, and the temperature of the hot water jet, measured inside of the nozzle, was kept at 32 °C. To capture the temperature distribution pattern of the hot water jet, mean water temperature measurements were carried out by moving a group of four temperature probes at different horizontal distances ($L$) downstream of the nozzle. The probes were positioned in a vertical line on the symmetry plane with a fixed spacing ($S$) between them. The described arrangement was chosen to minimize flow disturbance during measurements due to the presence of temperature probes. Temperature measurements were conducted using the EL-SGD 43-ATP, a four-channel temperature data logger equipped with real-time readings, trend graphing, and data analysis tools. Each probe, EL-PROBE2–1.0M-TP, measured 20 *mm* in length with a thickness of 3.5 *mm* and a temperature accuracy of ±0.5 °C within a temperature range of −10 °C to 70 °C. These probes were calibrated prior to testing and were attached to metal rods with a thickness of 1 *mm*. A fork-shaped structure, featuring two parallel plexiglass columns with a series of holes spaced at specific intervals ($d = 0.9$ *cm*), was designed to fix the metal rods at various heights from the flume bottom, as depicted in Fig. 19a and Fig. 19b. This structure was mounted on a dolly on top of the flume, allowing it to move along the flume length. At each specified distance from the nozzle, the spacing between the probes was arranged to ensure comprehensive coverage of the jet plume cloud, as detailed in Table 14. The experiment was repeated three times, and measurements were taken for one minute at each point, with the average values subsequently calculated.

**Table 14**
Position of the temperature measurement points at the symmetry plane of the flume and downstream of the nozzle.

| Horizontal distance of the probes from the nozzle outlet ($L/d$) | Spacing between the probes ($S/d$) | Vertical distance ($V$) of the lowest probe from the nozzle outlet ($V/d$) |
|---|---|---|
| 4 | 3 | 2 |
| 6 | 3 | 2 |
| 8 | 3 | 2 |
| 10 | 4 | 3 |
| 14 | 6 | 3 |
| 18 | 6 | 3 |
| 22 | 8 | 3 |

The hydro-thermal model was applied to replicate the results of the experiment in the modelling of the buoyant hot-water jet under current-wave coexisting conditions. A three-dimensional computational domain measuring 15 *m* in length, 0.6 *m* in width, and 0.8 *m* in depth was considered. The inclined pipe jet outlet was located at the symmetry plane and positioned 9 *m* from the inlet boundary condition, as shown in Fig. 20a. The mesh was generated using the snappyHexMesh technique, and a mesh dependency study was carried out with three different mesh sizes. The centreline path of the jet for the cases for the mean flow velocity are compared as shown in Fig. 21. The findings indicate that the mesh resolution was satisfactory for all mesh configurations, as there were no discernible significant differences in the results. A computational domain with roughly 2.6 million mesh cells was chosen for subsequent simulations. Fig. 20b showed part of the generated mesh around the area of the interest near the nozzle in the $x$-$z$ plane. A cell stretching wave damping technique was used in last 4 *m* of the mesh to ensure wave

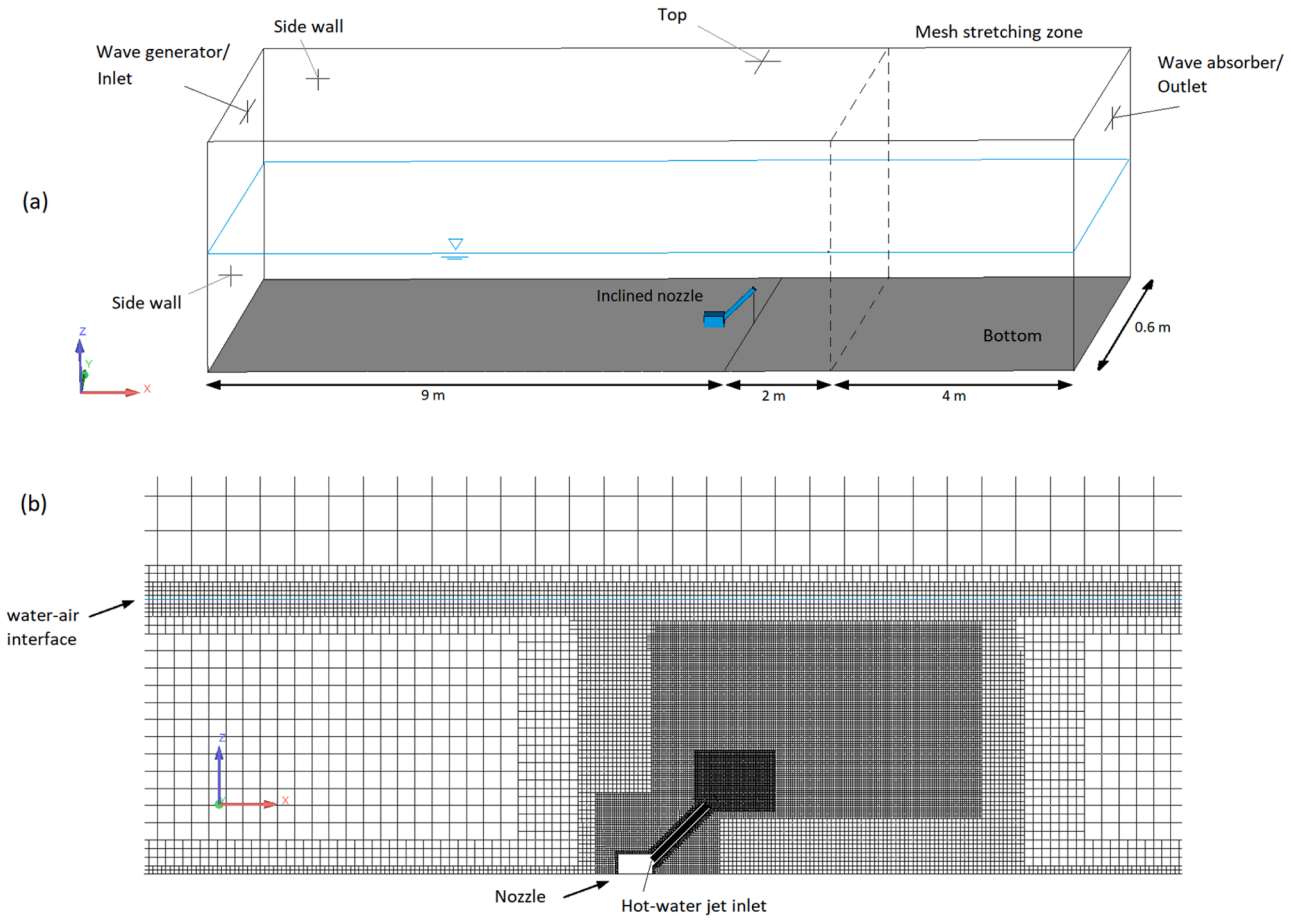


**Fig. 20.** (a) schematic of the computational domain and (b) part of the generated mesh in ***x-z*** plane for inclined buoyant hot-water jet under current-wave environment.

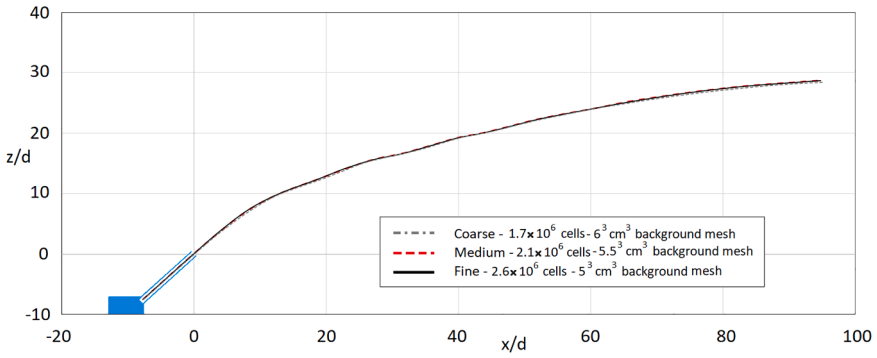


**Fig. 21.** Centreline path of the jet of the three generated meshes for inclined buoyant hot-water jet under current-wave environment case.

**Table 15**
Applied boundary conditions for temperature parameter in buoyant hot-water jet under current-wave condition.

| Boundaries | Hot-water jet inlet | Side walls | Top (patch/ atmospheric) | Bottom/ Nozzle wall (no-slip wall) | Inlet (wave generator) | Outlet (wave absorber) |
|---|---|---|---|---|---|---|
| Temperature ($T$) | Fixed Value | Symmetry | inletOutlet | ZeroGradient | fixedValue | inletOutlet |

reflections were suppressed. k-ω SST-multiphase was chosen for turbulence closure modelling.

The adopted boundary conditions for all flow parameters (except for temperature) were as those defined in Table 10, while the applied boundary conditions for temperature were provided in Table 15. To mimic the velocity profile of the water jet outlet, the boundary for the hot-water jet was defined 0.11 $m$ inside the nozzle outlet.

The mean temperature distribution field for simulation and experimental results was compared in Fig. 22. A noticeable discrepancy between the experimental and numerical results was observed at a measurement point very close to the centreline of the water jet outlet (at the point with measured temperature of $T$= 22.4°). The main reason for

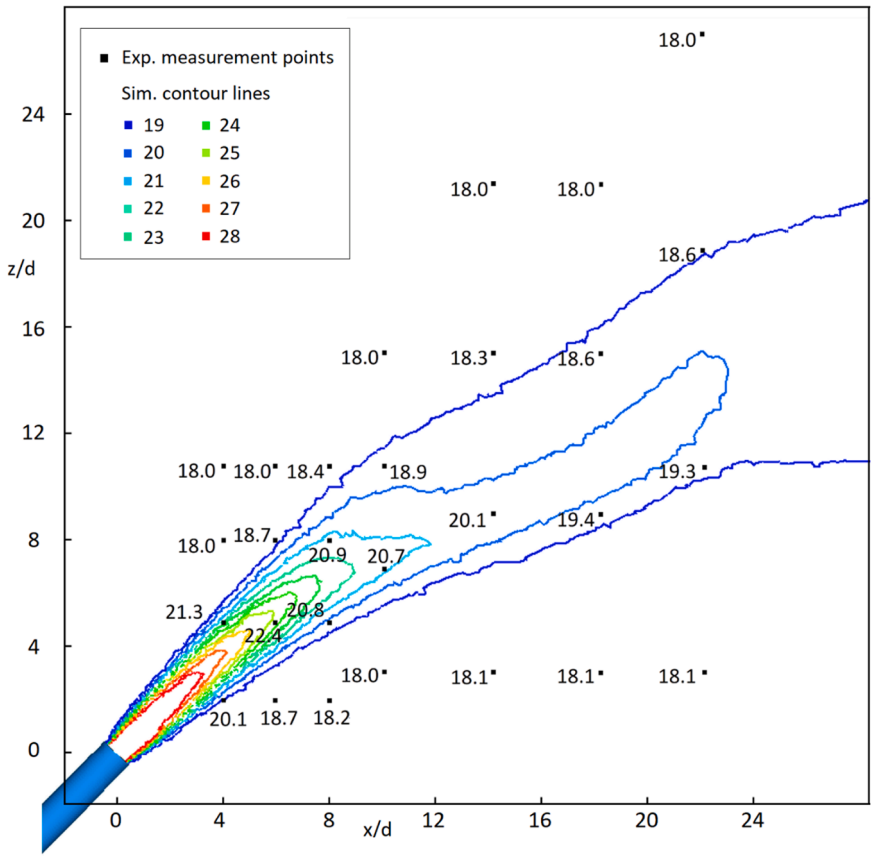


**Fig. 22.** Comparison of the mean temperature distribution field in ( °C) between numerical and experimental results on symmetry Plane downstream of the Nozzle.

this difference was the inaccuracy of experimental measurements in close proximity to the nozzle jet outlet, where the plume jet diameter was relatively thin compared to the size of the probes. Nevertheless, the results reveal that the model was remarkably capable of predicting the temperature field and distribution pattern of the hot water jet mixing zone under current-wave coexisting conditions.

Plume tracking was also performed using Eq. (18) by solving the concentration equation. Fig. 23 presents a comparison between the instantaneous flow pattern that resulted from the injection of dye in the water jet in the experimental test with the isosurfaces of the instantaneous concentration profile of the simulation result for current-wave conditions at different time periods of the wave. Again, apart from the identified higher diffusion rate near the discharge outlet, the developed numerical model precisely estimates most of the flow characteristics in terms of shape, hight and location of the mixing jet for the buoyant hot-water jet under the current-wave environment.

## 4. Conclusion

A novel three-dimensional discharge dispersion model for evaluating the near-field dilution, trajectory, and temperature distribution of thermal-induced buoyant water jet under the shallow coastal water condition was developed. The model solved the governing fluid flow and energy equations for two immiscible and incompressible phases (e.g. water-air) which were weakly coupled by applying Boberbeck-Boussinesq approximation. Different turbulence models, such as k−ε Multiphase, k-ω SST, k-ω SST-multiphase, k-ω SST-stable, realizable k−ε, were tested. k-ω SST turbulence model was chosen for its proven capability in predicting adverse pressure gradient and separating flow [35]; k−ε multiphase, k-ω SST-multiphase are modified version of the k−ε, k-ω SST for multiphase flow system, respectively [29]. k-ω SST-stable turbulence closure model was selected for its capability on predicting wave surface elevations, as well as turbulence and undertow velocity profiles [36], and the realizable k−ε model was reliable in capturing phenomena such as the Coanda effect, buoyant, and non-buoyant jets in stagnant environments [50,51].

Extensive verification of the model's performance was conducted by comparing the developed model against a diverse range of analytical and experimental data, both conducted experimentally and those from literature. First, a series of simulations were carried out to evaluate the performance of the model in reproducing the results of the wave hydrodynamic and interactions with the submerged trapezoid bar. This was followed by numerically replicating the experimental results of the non-buoyant submerged jet under current-only and current-wave environments. Then, the potency of the coupled hydro-thermal algorithm was assessed by validating the model against different thermal-induced buoyant submerged jet experimental tests. For this purpose, the results of a series of tests for the thermal-induced buoyant submerged horizontal jets in stationary water were conducted. Finally, the developed model was employed to an ultimate experimental test which is conducted at the coastal laboratory at the University of Plymouth for an inclined thermal-induced buoyant water jet under the current-wave environment.

Overall, analysing the results illustrated that among all, the simulation results of k-ω SST-multiphase provides remarkable agreement with the laboratory measurement data in terms of flow and temperature distribution field and plume trajectory and dilution. The findings confirmed that the developed model can be used as a reliable numerical tool in the precise prediction of characteristic thermal-induced buoyant water jet under current-wave coexistence. This contributed to better appreciation of the behaviour such as shallow water WTEBS effluent plume, and mixing zone for achieving maximum effluent mixing efficiencies.

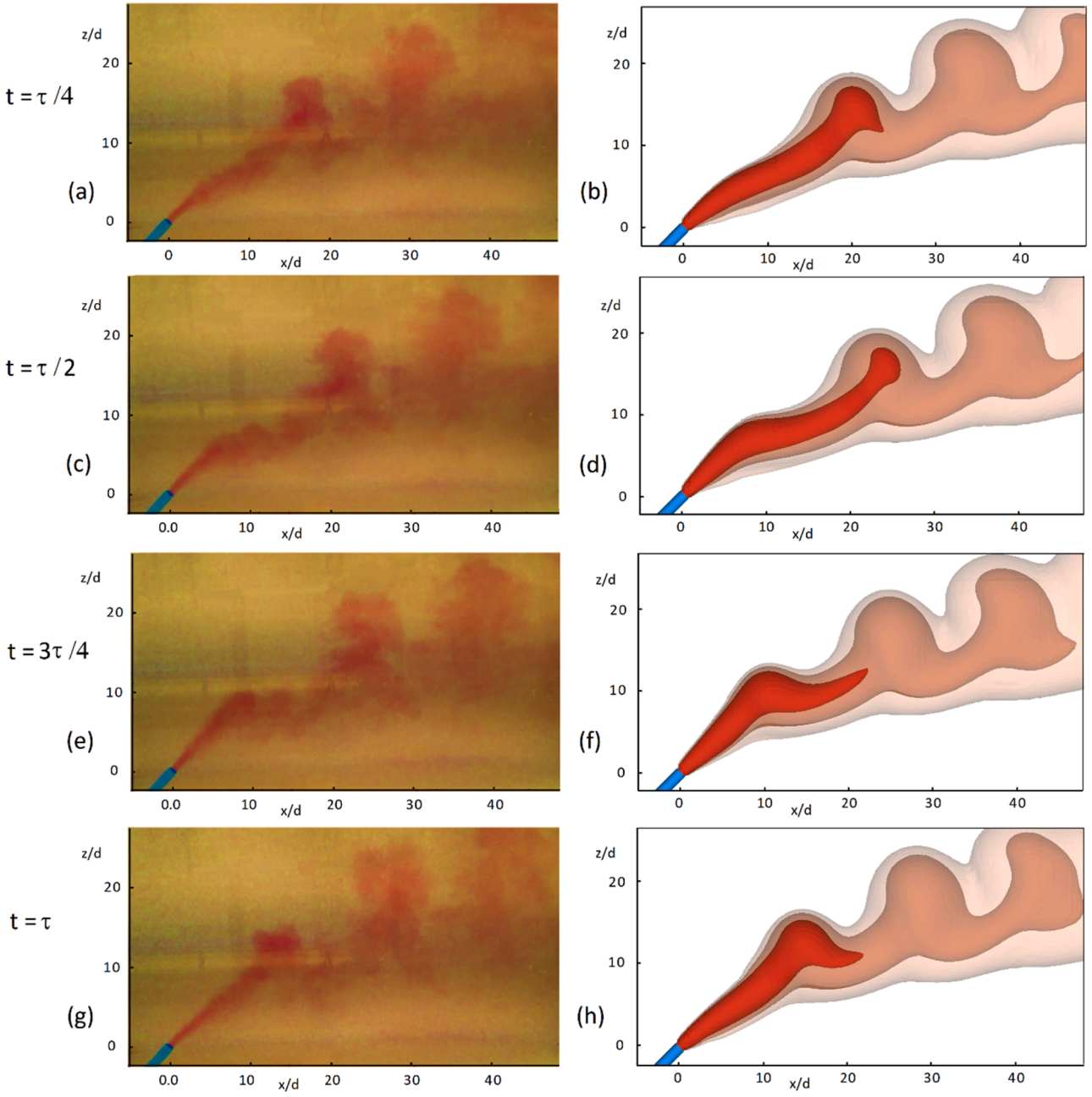


**Fig. 23.** Comparison of the instantaneous concentration profile of submerged hot water jet between the experimental and numerical results under current-wave coexisting condition at different time period of the wave: (a, b) $t = \tau/4$, (c, d) $t = \tau/2$, (e, f) $t = 3\tau/4$, (g, h) $t = \tau$.

## CRediT authorship contribution statement

**Amir Bordbar:** Writing – review & editing, Writing – original draft, Visualization, Validation, Supervision, Software, Resources, Project administration, Methodology, Investigation, Formal analysis, Data curation, Conceptualization. **Yong Ming Dai:** Writing – review & editing, Supervision. **Simone Michele:** Writing – review & editing, Supervision. **Ola Zawalna-Geer:** Writing – review & editing. **Zhengwei Chen:** Writing – review & editing. **Salah A Faroughi:** Writing – review & editing. **Yeaw Chu Lee:** Writing – review & editing, Writing – original draft, Supervision, Resources, Methodology, Funding acquisition, Conceptualization.

## Declaration of competing interest

The authors declare that they have no known competing financial interests or personal relationships that could have appeared to influence the work reported in this paper.

## Data availability

Data will be made available on request.

## Acknowledgements

The authors would like to acknowledge the support received from EUROSWAC (Project number 216) funded by Interreg France (Channel)

England program and European Regional Development Fund (ERDF), and Engineering and Physical Science Research Council (EPSRC) High End Computing Consortium for Wave Structure Interaction HEC WSI, EP/X035751/1.

## References


[1] G.W. BOEHLERT, A.B. GILL, Environmental and ecological effects of ocean renewable energy development: a current synthesis, Oceanography 23 (2010) 68–81.
[2] C.M. COMFORT, M.A. MCMANUS, S.J. CLARK, D.M. KARL, C.E. OSTRANDER, Environmental properties of coastal waters in Mamala Bay, Oahu, Hawaii, at the future site of a seawater air conditioning outfall, Oceanography 28 (2015) 230–239.
[3] C.M. COMFORT, L. VEGA, Environmental Assessment For Ocean Thermal Energy Conversion in Hawaii: Available data and a Protocol For Baseline monitoring. OCEANS'11 MTS/IEEE KONA, IEEE, 2011, pp. 1–8.
[4] A. BORDBAR, K. GEORGOULAS, Y.M. DAI, S. MICHELE, F. ROBERTS, N. CARTER, Y.C. LEE, Waterbodies thermal energy based systems interactions with marine environment—A review, Energy Reports 9 (2023) 5269–5286.
[5] K. ELAHEE, S. JUGOO, Ocean thermal energy for air-conditioning: case study of a green data center, Energy Sources, Part A: Recovery, Utilization, and Environmental Effects 35 (2013) 679–684.
[6] J. LILLEY, D.E. KONAN, D.T. LERNER, Cool as a (sea) cucumber? Exploring public attitudes toward seawater air conditioning in Hawai 'i, Energy Res. Soc. Sci. 8 (2015) 173–183.
[7] R. PELC, R.M. FUJITA, Renewable energy from the ocean, Mar. Policy. 26 (2002) 471–479.
[8] Z. XU, Y. CHEN, Y. WANG, C. ZHANG, Near-field dilution of a turbulent jet discharged into coastal waters: effect of regular waves, Ocean Engineering 140 (2017) 29–42.
[9] L. ZHEN, D. LIN, H. SHU, S. JIANG, Y. ZHU, District cooling and heating with seawater as heat source and sink in Dalian, China, Renew. Energy 32 (2007) 2603–2616.
[10] J. YU, Z. LIU, Y. LI, Optimization of Thermal Discharge Scheme for the Phase II Project of Rizhao Power Plant, 2009 Asia-Pacific Power and Energy Engineering Conference (2009) 1–4.
[11] Y.-P. CHEN, C.-W. LI, C.-K. ZHANG, Z.-S. XU, Numerical study of a round buoyant jet under the effect of JONSWAP random waves, China Ocean Engineering 26 (2012) 235–250.
[12] P. PAT GRANDELLI, G. ROCHELEAU, J. HAMRICK, M. CHURCH, P.D. BRIAN POWELL, Modeling the Physical and Biochemical Influence of Ocean Thermal Energy Conversion Plant Discharges Into Their Adjacent Waters, Makai Ocean Engineering, Inc, 2012.
[13] KIM, J. & KIM, H.-J. 2014. Numerical Modeling Of OTEC Thermal Discharges In Coastal Waters.
[14] J.H.-W LEE, V.H CHU, Turbulent Jets and plumes: a Lagrangian approach, Springer Science & Business Media, 2003.
[15] W.E. FRICK, Visual Plumes mixing zone modeling software, Environmental Modelling & Software 19 (2004) 645–654.
[16] G.H. JIRKA, R.L. DOMEKER, Hydrodynamic classification of submerged single-port discharges, Journal of hydraulic engineering 117 (1991) 1095–1112.
[17] Z. XU, Y. CHEN, J. TAO, Y. PAN, D.M. SOWA, C.-W. LI, Three-dimensional flow structure of a non-buoyant jet in a wave-current coexisting environment, Ocean Engineering 116 (2016) 42–54.
[18] Z. XU, Y. CHEN, Y. PAN, Initial dilution equations for wastewater discharge: example of non-buoyant jet in wave-following-current environment, Ocean Engineering 164 (2018) 139–147.
[19] Z. XU, E. OTOO, Y. CHEN, H. DING, 2D PIV measurement of twin buoyant jets in wavy cross-flow environment, Water. (Basel) 11 (2019) 399.
[20] S. FANG, Y. CHEN, Z. XU, Wave and current effects on a buoyant jet: an integral model, in: 38th IAHR World Congress, 2019, pp. 6142–6147.
[21] H. RUSCHE, Computational Fluid Dynamics of Dispersed Two-Phase Flows At High Phase Fractions, Imperial College London (University of London, 2003.
[22] H.G. WELLER, G. TABOR, H. JASAK, C. FUREBY, A tensorial approach to computational continuum mechanics using object-oriented techniques, Computers in physics 12 (1998) 620–631.
[23] J.H. FERZIGER, M. PERIĆ, R.L STREET, Computational Methods For Fluid Dynamics, Springer, 2002.
[24] R.I. ISSA, Solution of the implicitly discretised fluid flow equations by operator-splitting, J. Comput. Phys. 62 (1986) 40–65.
[25] N.G. JACOBSEN, D.R. FUHRMAN, J FREDSØE, A wave generation toolbox for the open-source CFD library: openFoam®, Int. J. Numer. Methods Fluids. 70 (2012) 1073–1088.
[26] P. HIGUERA, J.L. LARA, I.J. LOSADA, Realistic wave generation and active wave absorption for Navier–Stokes models: application to OpenFOAM®, Coast. Eng. 71 (2013) 102–118.
[27] F.J. MÉNDEZ, I.J. LOSADA, M.A LOSADA, Wave-induced mean magnitudes in permeable submerged breakwaters, Journal of Waterway, Port, Coastal and Ocean Engineering 127 (2001) 7–15.
[28] P. HIGUERA, J.L. LARA, I.J. LOSADA, Simulating coastal engineering processes with OpenFOAM®, Coast. Eng. 71 (2013) 119–134.
[29] P. HIGUERA, phicau/olaFlow: CFD for waves (v1.1), Zenodo (2018).
[30] M. MOHSENI, C.G. SOARES, Numerical investigation of inline wave force on a truncated vertical cylinder with different cross-sections in regular head waves, Ocean Engineering 251 (2022) 111063.
[31] J. CONDE, Comparison of different methods for generation and absorption of water waves, Revista de Engenharia Térmica 18 (2019) 71–77.
[32] H.E. HAFSTEINSSON, Porous Media in OpenFOAM, Chalmers University of Technology, Gothenburg, 2009.
[33] M.H. DAO, L.W. CHEW, Y. ZHANG, Modelling physical wave tank with flap paddle and porous beach in OpenFOAM, Ocean Engineering 154 (2018) 204–215.
[34] B LE MÉHAUTÉ, An Introduction to Hydrodynamics and Water Waves, Springer Science & Business Media, 2013.
[35] MENTER, F.R. 1.992. Improved two-equation k-omega turbulence models for aerodynamic flows.
[36] B.E. LARSEN, D.R. FUHRMAN, On the over-production of turbulence beneath surface waves in Reynolds-averaged Navier–Stokes models, J. Fluid. Mech. 853 (2018) 419–460.
[37] T. CEBECI, P. BRADSHAW, Momentum transfer in boundary layers, Washington (1977).
[38] T. CEBECI, K. CHANG, Calculation of incompressible rough-wall boundary-layer flows, AIAA Journal 16 (1978) 730–735.
[39] X. NI, W. FENG, S. HUANG, Y. ZHANG, X. FENG, A SPH numerical wave flume with non-reflective open boundary conditions, Ocean Engineering 163 (2018) 483–501.
[40] M. KARIMIRAD, Z. JIANG, Mechanical-dynamic loads. *Earth Systems and Environmental Sciences*, Elsevier, 2021.
[41] O.M. FALTINSEN, J. NEWMAN, T. VINJE, Nonlinear wave loads on a slender vertical cylinder, J. Fluid. Mech. 289 (1995) 179–198.
[42] R.G. DEAN, R.A. DALRYMPLE, Water Wave Mechanics For Engineers and Scientists, world scientific publishing company, 1991.
[43] M. RAHMAN, Fundamentals concerning Stokes waves, WIT Transactions on Engineering Sciences (1970) 9.
[44] Y.S. LI, S.-X. LIU, Y.-X. YU, G.-Z. LAI, Numerical modelling of multi-directional irregular waves through breakwaters, Appl Math Model 24 (2000) 551–574.
[45] S. BEJI, J. BATTJES, Numerical simulation of nonlinear wave propagation over a bar, Coast. Eng. 23 (1994) 1–16.
[46] S. BEJI, J. BATTJES, Experimental investigation of wave propagation over a bar, Coast. Eng. 19 (1993) 151–162.
[47] Y.-C. LI, J.B. HERBICH, Effect of Wave–Current Interaction on the Wave Parameter, Coast. Eng. 1982 (1982).
[48] R.J. SOBEY, A.J. JOHNSTON, R.D. KEANE, Horizontal round buoyant jet in shallow water, Journal of Hydraulic Engineering 114 (1988) 910–929.
[49] W.-X. HUAI, Z.-W. LI, Z.-D. QIAN, Y.-H. ZENG, J. HAN, W.-Q. PENG, Numerical simulation of horizontal buoyant wall jet, Journal of Hydrodynamics 22 (2010) 58–65.
[50] H. KHEIRKHAH GILDEH, A. MOHAMMADIAN, I. NISTOR, H. QIBLAWEY, Numerical modeling of turbulent buoyant wall jets in stationary ambient water, Journal of Hydraulic Engineering 140 (2014) 04014012.
[51] H. KHEIRKHAH GILDEH, A. MOHAMMADIAN, I. NISTOR, H. QIBLAWEY, Numerical modeling of 30 and 45 degree inclined dense turbulent jets in stationary ambient, Environmental Fluid Mechanics 15 (2015) 537–562.